

We are IntechOpen, the world's leading publisher of Open Access books Built by scientists, for scientists

6,300

Open access books available

171,000

International authors and editors

190M

Downloads

Our authors are among the

154

Countries delivered to

TOP 1%

most cited scientists

12.2%

Contributors from top 500 universities



WEB OF SCIENCE™

Selection of our books indexed in the Book Citation Index
in Web of Science™ Core Collection (BKCI)

Interested in publishing with us?
Contact book.department@intechopen.com

Numbers displayed above are based on latest data collected.
For more information visit www.intechopen.com



Mathematical Modeling and Simulation of Rapeseed Drying on Concurrent-Flow Dryer

Le Anh Duc and Keum Dong Hyuk

Abstract

Mathematical modeling for rapeseed drying on concurrent-flow dryer was built based on energy and mass transfer balances. The fourth-order Runge–Kutta method was used for solving four ordinary differential equations. A computer simulation program for circulating concurrent-flow rapeseed dryer was developed using these models. A pilot-scale concurrent-flow dryer was used to verify the fitness of simulation program. Two drying experiments were conducted. The output parameters of the simulation program were compared and analyzed with experiment data. The RMSE of simulated moisture contents ranged from 0.334 to 0.506%w.b. with the coefficient of determinations ranged from 0.994 to 0.997. The RMSE of simulated rapeseed temperatures during drying process ranged from 1.15 to 1.77°C with the R^2 ranging from 0.904 to 0.925. The experimental drying rates were 2.38 and 2.80% w. b./h. In comparison with simulated values, the difference between simulated value and measured value of drying rate were 5.04 and 5.08%; drying time were 7.14 and 0.47%; and germination ratio were 1.87 and 0.47%. The simulated fuel energy consumption for drying were 4.62 and 8.57% lower than the experimental values. The analytic results showed that the simulation results have good fitness with experimental data.

Keywords: concurrent-flow dryer, mathematical modeling, simulation, drying rate, grain temperature, moisture content

1. Introduction

There are many different grain dryer designs on the market. Basically, the classical configurations of the moving bed dryers fall into four categories according to the relative directions of seed and air flows: the mixed flow dryer, the cross flow dryer, the concurrent-flow dryer, and the countercurrent flow dryer. The configuration with parallel concurrent-flow displays some advantages, such as obtaining of more homogeneous products as well as a better energy usage.

Concurrent-flow drying is a relatively new grain drying technology. In a concurrent-flow dryer, both the grain and drying air are moving in the same direction. This type of dryer has the advantage of using very high drying air temperatures without affecting grain quality and does not suffer the variation in grain moisture contents. Besides, energy efficiency of this type dryer is high.

The concurrent-flow drying principle was introduced the first time in 1955 by Öholm. Thompson et al. [1] developed simulation models of concurrent-flow dryer for corn drying. Now most of the drying simulation model was implemented based on the model presented by Thompson et al. that was developed for simulating high temperature corn drying. Felipe and Barrozo [2] studied the simultaneous heat and mass transfer between air and soybean seeds in a concurrent moving bed dryer, based on the application of a two-phase model to the drying process. Keum et al. [3] studied on circulating concurrent flow for rice drying with the drying temperature from 98 to 126°C, and air flow rate from 28.5 to 57.1 cmm/m². The study results showed that drying rate ranged from 1.09 to 2.2% d.b./h, and energy consumption ranged from 6224 to 6992 kJ/kg-water.

From these advantages, the use of concurrent-flow drying principle for drying of rapeseed has been recommended owing to:

- Energy saving: energy efficiency of this type dryer is about 30–40% better than a cross flow type dryer without heat recovery.
- It is possible to use a high drying temperature (up to 130°C) without increasing the grain temperature excessively because grain are exposed to drying air in a short time, leads to high drying rate (1.5–2% w.b./h).
- The drying air flow is parallel to the grain flow leads to more homogeneous moisture content and temperature distributions because all grains are exposed to the same temperatures, therefore guaranteeing the quality of the dried grains.

Mathematical modeling and computer simulation can be used to predict the moisture and temperature of the products during the drying process and the energy consumption and drying capacity of the different drying system. Many different models have been proposed to describe the drying process in the basic types of convective grain dryer. However, no previous research was found in literature that study on dynamic simulation of concurrent flow for rapeseed.

2. Concurrent-flow drying model

2.1 Selection of drying principle

The drying process of rapeseed in concurrent-flow dryer was described in **Figure 1**.

The hot air and rapeseed are moving the same direction in the drying chamber. At the end of cycle drying, hot air is exhausted to ambience by suction fan; rapeseed is continued to be circulated on the drying chamber for the next cycle drying until it reaches the desired final moisture content.

2.2 Mathematical model

The mathematical model used in the study consists of a set of four partial differential equations in four independent variables: air humidity, air temperature, grain temperature, and grain moisture content.

Based on the theory of energy and mass transfer, a concurrent-flow rapeseed drying model was developed. By using this mathematical models, performance of concurrent-flow rapeseed dryer can be predicted; the temperature and moisture

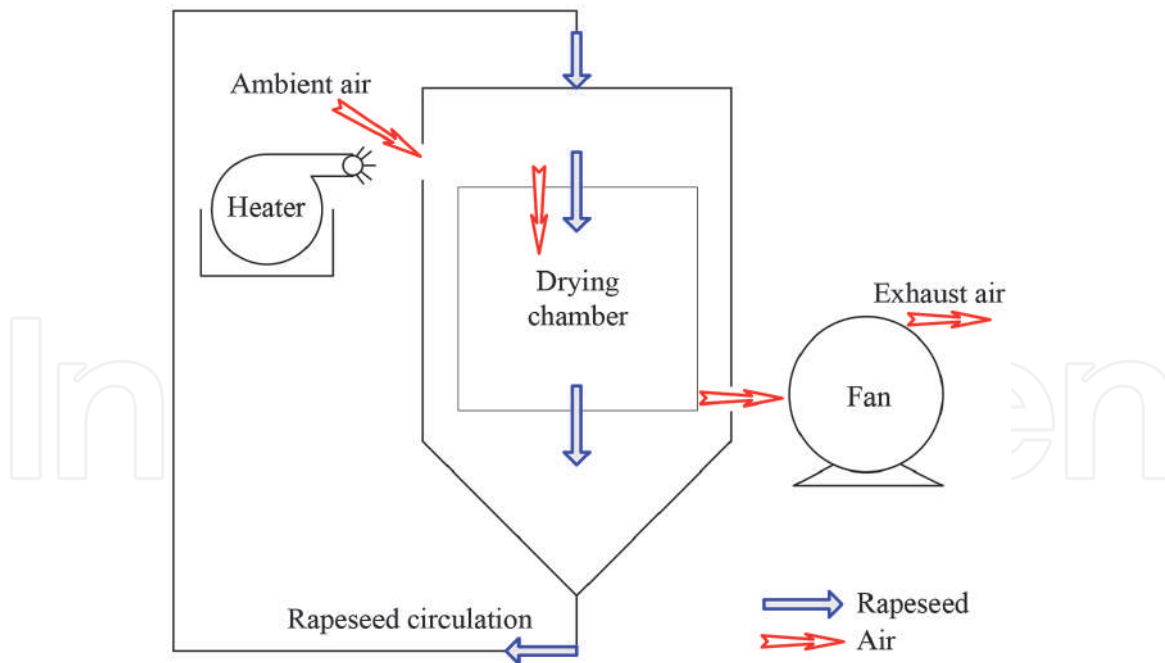


Figure 1.
 Block diagram of rapeseed concurrent-flow dryer.

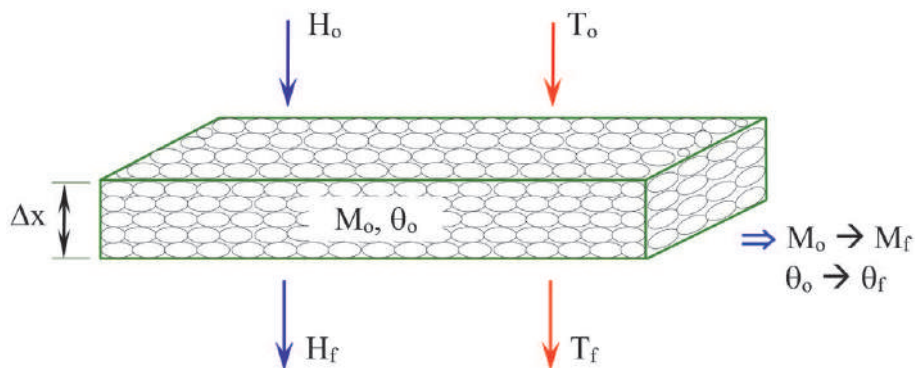


Figure 2.
 Concurrent-flow drying model.

content of rapeseed and the temperature and relative humidity of drying air were predicted.

The thin layer drying models is used in simulation of deep-bed dryer, in which the average changes in moisture content and temperature on a thin layer of grain are calculated over a discrete time interval Δt . In the simulation, to solve mathematical models of deep-bed drying process, the depth bed was divided into n th thin layers with a thickness of Δx each, and dynamic heat and mass balances were set up in each section, and then the model consisted in a set of partial differential equations (**Figure 2**). Drying is achieved by continuously passing hot air through the static grain bed in one direction, from the top to the bottom section. From the first thin layer at the top section, the air evaporates moisture from the grain and carries it to the next thin layer. As the drying air absorbs moisture, its temperature is decreased, and its ability to pick up more moisture (drying potential) decreases. A deep bed consisting of a number of thin layers is, therefore, simulated by calculating the air and moisture changes as the drying air passes from one thin layer of grain to the next layer. Each layer dries to equilibrium conditions for short time intervals, and the exhaust air from one layer is used as the input drying air to the next. The drying procedure continues for a number of drying time intervals until the desired final moisture content of the material is achieved.

Some of these assumptions are made to simplify the mathematical model. So, for developing these mathematical models, the following assumptions were made:

- Operation is in the steady state.
- Grain shrinkage is negligible during the drying process.
- No temperature gradients exist within each grain particle.
- Particle-to-particle conduction is negligible.
- Initial moisture content of grain is uniform.
- Airflow and grain flow are plug-type and constant.
- The dryer walls are adiabatic and heat losses are negligible.
- The heat capacities of moist air and of grain are constant during the short time periods.
- The solids flow rate is uniform.

Energy balances and mass balances are written on a differential volume ($S \cdot \Delta x$) located at an arbitrary location in the grain bed. There are four unknowns in this problem:

$T(x,t)$: the air temperature.

$\theta(x,t)$: the grain temperature.

$H(x,t)$: the humidity ratio.

$M(x,t)$: the grain moisture content.

Therefore, four equations for material and energy balances must be made in order to calculate of T , θ , H , and M . Resulting from the balances are four Eq. (4):

1. For the enthalpy of the air (air enthalpy balance):

The change in sensible heat of air that results due to heat transfer by convection in time. The air enthalpy balance over the differential volume:

energy out = energy in – energy transferred by convection

$$\frac{dT}{dx} = \frac{-h_c a}{G_a c_a + G_a c_v H} (T - \theta) \quad (1)$$

2. For the enthalpy of the grain (grain enthalpy balance):

The enthalpy from the air to the grains due to convection heat transfer over the control volume is equal to the required heat to evaporate water inside the grains and to heat water vapor extracted from the grains and the rate of accumulated heat inside the grains. The grain enthalpy balance over the differential volume:

energy transferred = change in internal grain energy – energy for evaporation

$$\frac{d\theta}{dx} = \frac{h_c a}{G_p (c_p + M c_w)} (T - \theta) - \frac{h_{fg} + c_v (T - \theta)}{G_p (c_p + M c_w)} G_a \frac{dH}{dx} \quad (2)$$

3. For the humidity of the air (humidity balance):

The amount of water in and out the differential volume is equal to the rate of change of moisture content in the grains.

moisture transferred = moisture in–moisture out

$$\frac{dH}{dx} = -\frac{G_p dM}{G_a dx} \quad (3)$$

4. For the moisture content of the grain (thin layer drying equation):

$$\frac{dM}{dx} = \text{an appropriate thin layer drying equation}$$

$$\frac{dM}{dx} = \frac{M_o - M_e}{v_p} (-Pt^{Q-1}Q) \exp(-Pt^Q) \quad (4)$$

where:

a: specific surface area of grain (m^2/m^3).

c_a : specific heat of dry air ($\text{kJ}/\text{kg}\cdot\text{K}$).

c_p : specific heat of dry grain ($\text{kJ}/\text{kg}\cdot\text{K}$).

c_v : specific heat of water vapor ($\text{kJ}/\text{kg}\cdot\text{K}$).

c_w : specific heat of water in grain ($\text{kJ}/\text{kg}\cdot\text{K}$).

G_a : air flow rate ($\text{kg}/\text{h}\cdot\text{m}^2$).

G_p : grain flow rate ($\text{kg}/\text{h}\cdot\text{m}^2$).

h_{fg} : vaporization latent heat of water within grain (kJ/kg).

H: enthalpy of dry air (kJ/kg).

h_c : convection heat transfer coefficient ($\text{kJ}/\text{h}\cdot\text{m}^2\cdot^\circ\text{C}$).

v_p : grain velocity (m/h).

Eqs. (1) and (2) represent the respective energy balances. Eqs. (3) and (4) result from mass balances applied for both fluid and solid phases of a concurrent-flow dryer.

The equation for the moisture content is obtained from the empirical thin layer equation for rapeseed. The four differential equations from (1)–(4) constitute the concurrent-flow drying model. A computer simulation program was developed using these models.

To solve these differential equations, the initial and boundary condition of grain and the drying air must be known and furnished to the simulation program as input data [4]. In this category fall:

- The initial or inlet temperature and moisture content of grain
- The initial or inlet temperature and absolute humidity of the drying air

The initial conditions of the air humidity, grain moisture, and both air and grains temperatures were assumed constant at the dryer inlet, resulting in the following model boundary conditions ($x = 0$) for concurrent-flow dryer which are:

$$T_{x=0} = T_{in} \quad (5)$$

$$\theta_{x=0} = \theta_o \quad (6)$$

$$H_{x=0} = H_{in} \quad (7)$$

$$M_{x=0} = M_o \quad (8)$$

where:

T_{in} : inlet air temperature ($^{\circ}\text{C}$).

θ_o : initial grain temperature ($^{\circ}\text{C}$).

H_{in} : inlet humidity ratio of drying air (kg/kg).

M_o : initial moisture content of grain (dec., d.b.)

2.3 Related equations

The related equations used for simulation such as specific surface area, latent heat, convection heat transfer coefficient, equilibrium moisture content, and thin layer drying equation of rapeseed were taken from specific studies.

2.3.1 Specific surface area of rapeseed

Specific surface area of rapeseed was determined in Eq. (9) [5]:

$$a = \frac{6(1 - \varepsilon)}{d} \quad (9)$$

where:

ε : void fraction was calculated based on bulk density and true density of rapeseed, $\varepsilon = 0.389$.

d : diameter of rapeseed was determined in our previous study, $d = 2.21 \times 10^{-3}$ m [6]. Then, the specific surface area of rapeseed is $a = 1659 \text{ m}^2/\text{m}^3$.

2.3.2 Latent heat

Gallaher [7] established the following equation Eq. (10) to determine the dependence of the latent heat of vaporization of water from the product on its moisture content:

$$h_{fg} = h_{fgo} \cdot [1 + A \cdot \exp.(-B \cdot M)] \quad (10)$$

h_{fg} : latent heat of vaporization of water in grain (kJ/kg-water).

h_{fgo} : latent heat of vaporization of free water (kJ/kg-water).

$$h_{fgo} = (2502.2 - 2.386 \cdot T)$$

T : drying air temperature ($^{\circ}\text{C}$).

M : rapeseed moisture content (decimal, d.b.)

A, B : coefficients.

The coefficients A and B were determined based on equilibrium moisture content of rapeseed (Modified Halsey equation) [8].

The values of the relative humidity can be replaced by equilibrium relative humidity (ERH) obtained from the equilibrium moisture content versus ERH relationships described in above section. Then:

$$P_v = P_s \cdot \text{ERH} \quad (11)$$

The relationship between vapor pressure and latent heats of two substances at the same temperature is as follows [5]:

$$\ln P_v = \frac{h_{fg}}{h_{fgo}} \ln P_s + C \quad (12)$$

where C is a constant of integration.

The ratio of heat of vaporization of water in grain to the heat of vaporization of saturated water on a logarithmic scale gives the ratio of latent heat h_{fg}/h_{fgo} at each level of moisture content as the slope of the straight line obtained from Eq. (12):

$$\frac{h_{fg}}{h_{fgo}} = 1 + A \cdot \exp(-B \cdot M) \quad (13)$$

Using MATLAB simulation program, the coefficients were found.

$$A = 0.3734.$$

$$B = 14.2442.$$

This result is fairly similar to the result of Cenkowski et al. [9]: A = 0.5; B = 14.5.
 Convection heat transfer coefficient [5]:

$$h_c = 0.277 \cdot G_a \cdot \left(\frac{d \cdot G_a}{\mu_a} \right) \quad (14)$$

where:

h_c : convection heat transfer coefficient of grain bed (kJ/h·m²·K).

d: geometric mean diameter of rapeseed (m).

μ_a : dynamic viscosity of air (kg/h·m).

$$\mu_a = 0.06175 + 0.000165 \cdot T \quad (15)$$

T: drying temperature (K).

Equilibrium moisture content [8]:

Equilibrium moisture content of rapeseed was determined using Modified Hal-sey equation:

$$M = [\exp(-4.9758 - 0.0132 \cdot T)]^{1/1.8755} (-\ln RH)^{-1/1.8755} \quad (16)$$

Thin layer drying [10]:

Thin layer drying equation of rapeseed was determined using model of Page:

$$MR = \exp(-P \cdot t^Q) \quad (17)$$

where the drying constants were determined:

$$P = 0.02246 + 3.2428 \cdot RH + 0.0006308 \cdot T^2 - 2.01481 \cdot RH^2 - 0.06077 \cdot T \cdot RH.$$

$$Q = 0.60932 - 1.72018 \cdot RH^2 + 0.02529 \cdot T \cdot RH.$$

2.4 Numerical solution

Eqs. (1)–(4) and the boundary conditions Eqs. (5)–(8) were solved using the Runge–Kutta methods.

In numerical analysis, the Runge–Kutta methods are an important family of iterative methods for the approximation of solutions of ordinary differential equations (ODEs). These techniques were developed around 1900 by the German mathematicians Runge C. and Kutta M.W. One member of the family of

Runge–Kutta methods that is so commonly used is the fourth-order Runge–Kutta method or also called as RK4, meaning that the error per step is on the order of h^5 , while the total accumulated error has order h^4 [11].

Let an initial value problem be specified as follows:

$$y' = f(y, t), y(t_0) = y_0 \quad (18)$$

where $f(t,y)$ is a function of y and t and the second equation is an initial condition.

In order to calculate y_{n+1} with a known value of y_n , integrate Eq. (18) in the interval $t_n \leq t \leq t_{n+1}$ to yield.

$$y_{n+1} = y_n + \int_{t_n}^{t_{n+1}} f(y, t) dt \quad (19)$$

The RK4 method is derived by applying a numerical integration method to the right side of Eq. (19). Then, the general form of the RK4 method for this problem is given by the following equations:

$$y_{n+1} = y_n + \frac{1}{6}(k_1 + 2k_2 + 2k_3 + k_4) \quad (20)$$

$$t_{n+1} = t_n + h \quad (21)$$

for $n = 0, 1, 2, 3, \dots$

$$k_1 = h \cdot f(y_n, t_n) \quad (22)$$

$$k_2 = h \cdot f\left(y_n + \frac{k_1}{2}, t_n + \frac{h}{2}\right) \quad (23)$$

$$k_3 = h \cdot f\left(y_n + \frac{k_2}{2}, t_n + \frac{h}{2}\right) \quad (24)$$

$$k_4 = h \cdot f(y_n + k_3, t_n + h) \quad (25)$$

h : size of the interval

Thus, the next value (y_{n+1}) is determined by the present value (y_n). The slope is a weighted average of slopes:

k_1 is the slope at the beginning of the interval.

k_2 is the slope at the midpoint of the interval, using slope k_1 to determine the value of y at the point $(t_n + h/2)$ using Euler's method.

k_3 is again the slope at the midpoint, but now using the slope k_2 to determine the y -value.

k_4 is the slope at the end of the interval, with its y -value determined using k_3 .

In averaging the four slopes, greater weight is given to the slopes at the midpoint:

$$slope = \frac{1}{6}(k_1 + 2k_2 + 2k_3 + k_4) \quad (26)$$

To solve mathematical models of drying process, the depth bed model was divided into 10 thin layers, and the dynamic heat and mass balances were set up in each section and calculated over a discrete time interval $\Delta t = 0.01$ h.

3. Simulation program

3.1 Main program

The numerical solution for four ordinary differential equations was obtained by using MATLAB code programs based on fourth-order Runge–Kutta methods. MATLAB is an interactive program and technical computing environment with numeric computation and data visualization. It provides integrated numerical analysis, matrix computation, signal processing, and graphics in an easy-to-use environment where problems and solutions are easily expressed without complicated programming. MATLAB-based software, entitled RCDSim-LAD (Rapeseed Concurrent-flow Drying Simulation, version LAD), was built for drying simulation.

The concurrent-flow dryer simulation model was programmed with the sequence:

- Input data
- Initialize arrays
- Evaluate constants
- Solve four ordinary differential equations
- Output when appropriate

The program of concurrent model terminates in one of two ways:

- When the moisture content within the dryer reaches a specified level
- When condensation or absorption is detected

However, condensation or absorption is not simulated in the concurrent model since it does not occur in a properly designed dryer. Equations used by more than one model (e.g., psychrometric equations) are programmed as separate subroutines of function subprogram. A computer simulation program was built using these models. This program was used in predicting the performance and temperature profile within the grain bed.

Input data	Output data
Initial grain condition:	Drying time (h)
• Initial grain moisture content (dec, w.b.)	Number of pass
• Initial grain temperature (°C)	Final moisture content (% w.b.)
• Desired final moisture content (dec,w.b.)	Drying rate (% w.b./h)
Dryer specification:	Water removal rate (kg/m ²)
• Capacity (kg)	Fan static pressure (Pa)
• Drying air flow rate (cmm/m ²)	Fan power (kW/m ²)
• Grain flow velocity (m/h)	Fan energy (kJ/kg-water)
Drying and ambient air condition:	Fuel energy (kJ/kg-water)
• Drying air temperature (°C)	Total energy consumption (kJ/kg-water)
• Ambient air temperature (°C)	
• Ambient air relative humidity (dec.)	

Table 1.
Input and output data in the simulation program.

Table 1 listed input data and output data which was simulated by a simulation program. The flow chart of the simulation program is shown in **Figure 3**. For the convenience, the interface graphical user interface (GUI) was built in **Figure 4**.

3.2 Energy consumption

3.2.1 Fuel energy consumption

$$EnFuel = \frac{G_a \cdot (c_a + c_v \cdot h) \cdot (T - T_{amb}) \cdot t}{0.85 \cdot (M_o - M_f) \cdot \rho_g \cdot x} \quad (27)$$

where:

EnFuel: fuel energy consumption (kJ/kg-water).

G_a : air flow rate (kg/h·m²).

c_a : specific heat of dry air (kJ/kg·K).

c_v : specific heat of water vapor (kJ/kg·K).

h : absolute humidity (kg-water/kg-dry air).

T : drying air temperature (°C).

T_{amb} : ambient air temperature (°C).

t : drying time (h).

M_o : initial moisture content (decimal, d.b.)

M_f : final moisture content (decimal, d.b.)

ρ_g : dry grain bulk density (kg/m³).

x : grain layer thickness (m).

3.2.2 Fan power

$$PFan = \frac{\Delta P \cdot g_a \cdot A}{60 \cdot e_f \cdot 1000} \quad (28)$$

where:

PFan: fan power (kW).

ΔP : pressure drop (Pa).

A : cross-section area of grain bed (m²).

g_a : air flow rate (m³/min·m²).

e_f : efficiency of the fan and motor (usually a value of about 0.5 is used).

3.2.3 Fan energy consumption

$$EnFan = \frac{PFan \cdot t \cdot 3600}{(M_o - M_f) \cdot \rho_g \cdot x} \quad (29)$$

where:

EnFan: fan energy consumption (kJ/kg-water).

3.2.4 Total energy consumption

$$EnTot = EnFuel + EnFan \quad (30)$$

where:

EnTot: total energy consumption (kJ/kg-water).

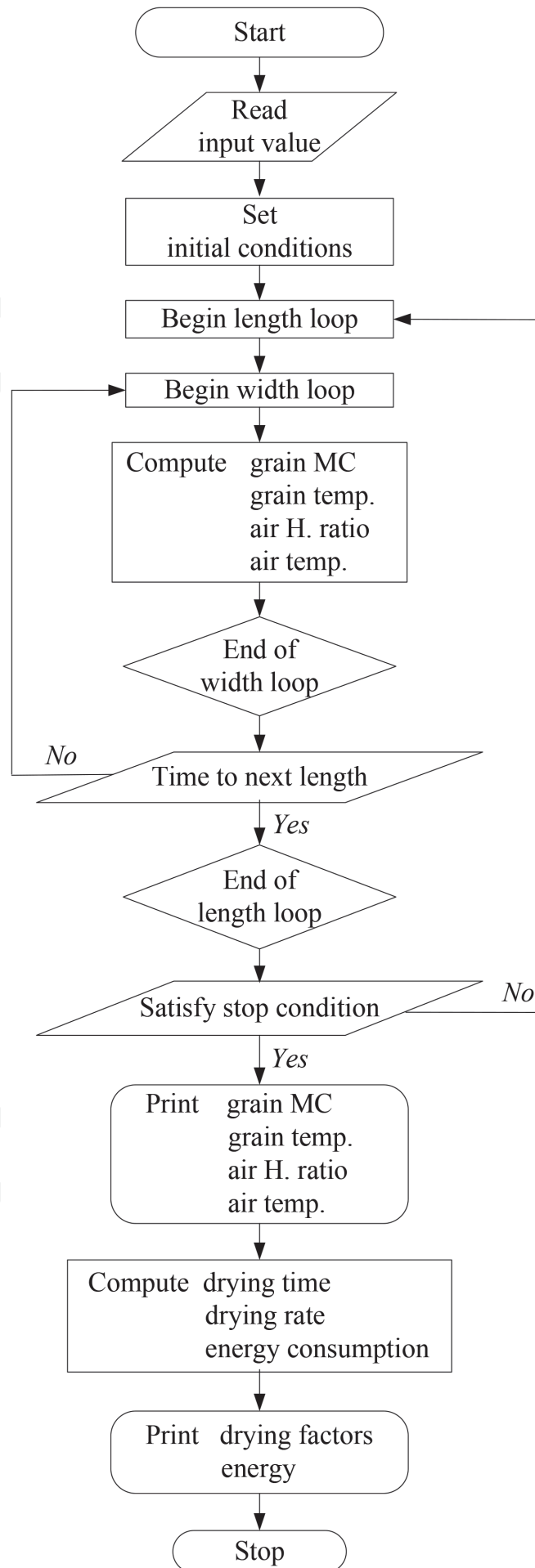


Figure 3.
Flow chart of the simulation program.

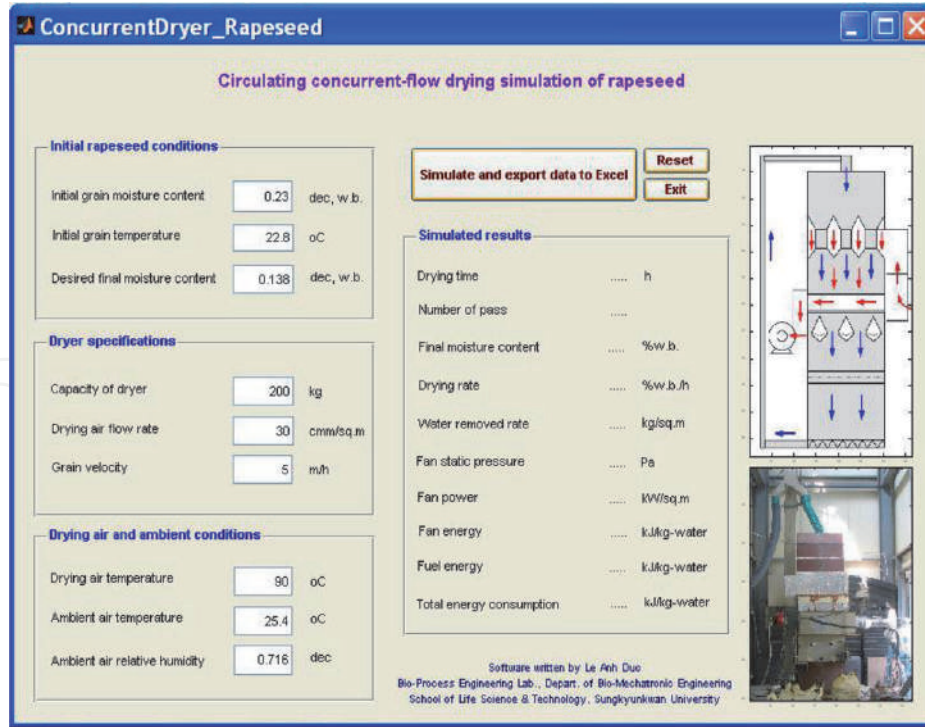


Figure 4. Interface of the simulation program RCDSim-LAD.

3.3 Psychrometric properties

3.3.1 Saturated vapor pressure

$$P_s = r \frac{a + b \cdot T_k + c \cdot T_k^2 + d \cdot T_k^3 + e \cdot T_k^4}{f \cdot T_k - g \cdot T_k^2} \quad (31)$$

where:

P_s : saturated vapor pressure (Pa).

T_k : absolute temperature (K).

$r = 22105649.25$; $a = -27405.526$; $b = 97.5413$; $c = -0.146244$;

$d = 0.12558 \times 10^{-3}$; $e = -0.48502 \times 10^{-7}$; $f = 4.34903$; $g = 0.39381 \times 10^{-2}$.

3.3.2 Absolute humidity

$$h = 0.6219 \cdot \frac{RH \cdot P_s}{P_{atm} - RH \cdot P_s} \quad (32)$$

h : absolute humidity (kg-water/kg-dry air).

RH : relative humidity (dec).

P_{atm} : atmospheric pressure, $P_{atm} = 101,325$ (Pa).

3.3.3 Specific volume

$$vs = 287 \cdot T_k \cdot \frac{0.6219 + h}{0.6219 \cdot P_{atm}} \quad (33)$$

vs : specific volume (m^3/kg).

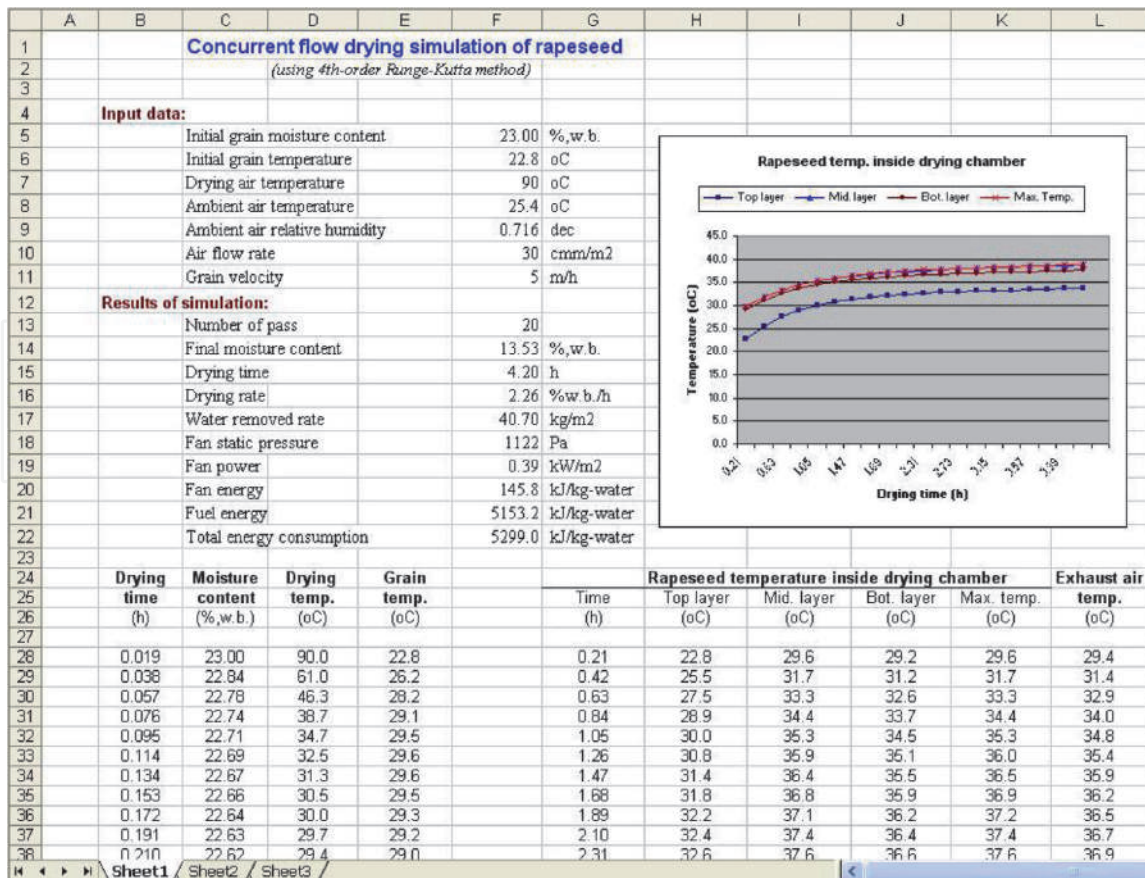


Figure 5. Simulated data with excel interface.

Using MATLAB 7.3.0., Simulated results were exported to Excel (Figure 5) by clicking the button “Simulate and export data to Excel” on the interface of the simulation program (Figure 4).

In excel interface, besides the output data in the simulation program were listed in Table 1, the drying air temperature, rapeseed temperature, and moisture content of rapeseed in the drying process versus drying time are also displayed and automatically represented by graphs, in which the rapeseed temperature at the top layer, middle layer, bottom layer, and the maximum rapeseed temperature in the drying chamber versus drying time are also displayed.

4. Model validation

4.1 Pilot-scale concurrent-flow dryer

In order to verify a fitness of simulation program, a pilot-scale concurrent-flow rapeseed dryer with capacity of 200 kg/batch was designed and manufactured. The dimension of the dryer is shown in Figure 6, and the structural principle of the dryer is shown in Figure 7. The pilot-scale rapeseed dryer includes a drying tower with grain inlet section, plenum section, and drying section; burner; drying fan; variable speed discharge augers; and bucket elevator for circulating the grains.

The hot air is supplied by a kerosene jet burner; after going through the mixed chamber, the drying air will enter the dryer through plenum section. Rapeseed and drying air are moving the same direction until drying the air out by force of suction

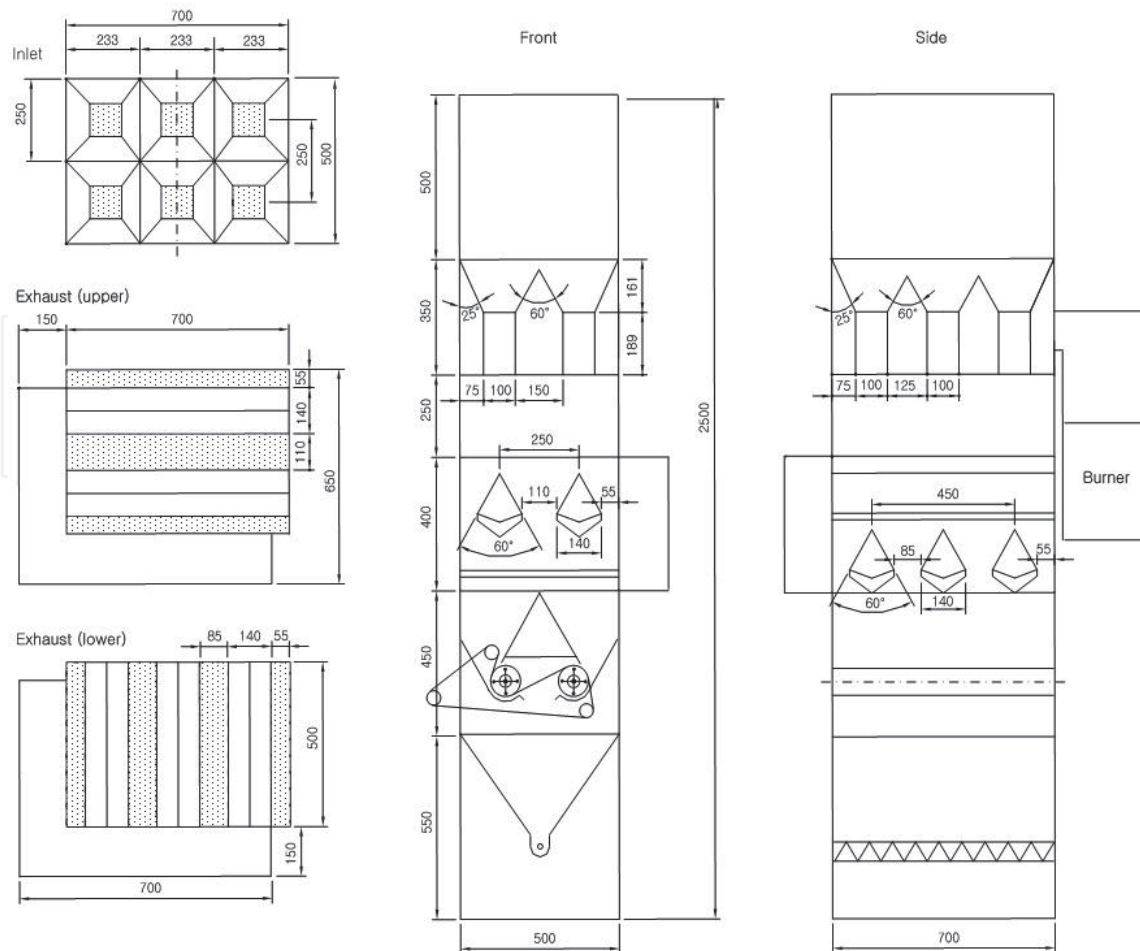


Figure 6.
Technical drawing of pilot-scale concurrent-flow dryer.

centrifugal fan through five exhaust air ducts. Rapeseed flow rate is controlled by two variable speed discharge augers. Rapeseed is out the dryer by discharge augers. Then, the grains are circulated by bucket elevator from the top of the dryer and flow down the vertical drying chamber.

The dimensions of the pilot-scale concurrent-flow dryer are shown in detail in **Figure 6**.

4.2 Experimental design

During the experiment the drying air temperature and grain temperature are continuously measured by temperature sensors (Thermocouple T-type, Omega, USA). The total of 16 temperature sensors was arranged at necessary positions inside and outside the dryer (**Figure 7**). Data from sensors were transferred to data logger system. Two computers were used to record the temperature data from the data logger (Datscan 7327, UK).

In the plenum section, drying air temperature input was measured by three sensors No. 1–3. In exhaust air ducts, two sensors at upper ducts (No. 10–11) and two sensors at lower ducts (No. 12–13) were arranged to measure exhaust air temperature. In the drying chamber, six sensors (No. 4–9) were arranged at six positions in the cross-section of the drying chamber to measure the temperature of grains. In two discharge augers, two sensors (No. 14–15) were arranged above the two discharge augers to measure discharge rapeseed temperature (rapeseed temperature after drying). To measure ambient air temperature, one temperature sensor (No. 16) was arranged outside the dryer (**Table 2**).

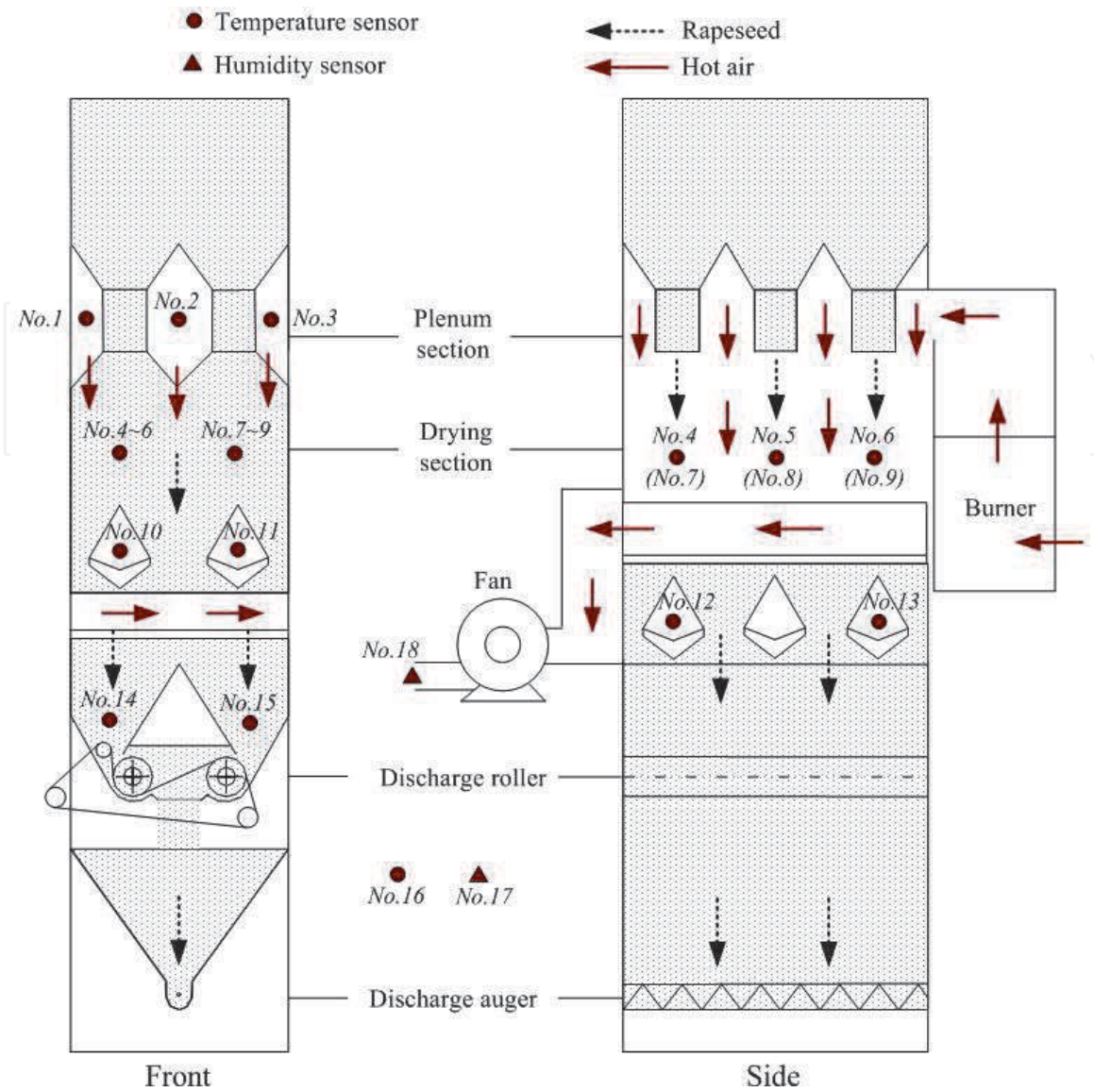


Figure 7. Design layout for the temperature and relative humidity sensor locations in the pilot-scale concurrent-flow dryer.

Temperature measurement		Sensors	
Drying air temperature	Inlet	3	No. 1-3
	Outlet	4	No. 10-13
Rapeseed temperature	Drying chamber	6	No. 4-9
	Discharge	2	No. 14-15
Ambient air temperature		1	No. 16
Relative humidity measurement			
Ambient air relative humidity		1	No. 17
Exhaust air relative humidity		1	No. 18

Table 2. Temperature sensors distribution and hygrometer used in the experiment.

Two hygrometers (MTH4100, Sanyo, UK, 10 – 99%, $\pm 2.5\%$) were installed to record the ambient air relative humidity (No. 17) and exhaust air relative humidity (No. 18) (Table 2).

In both experiments, grain flow velocity was set up at 5 m/h; this value is equivalent to the mass of circulated rapeseed which is 1000 kg/h. The grain flow velocity is controlled by two discharge rollers. The rotation of discharge rollers was 3.5 rpm. The rotation of discharge rollers was controlled by an inverter (S500, Mitsubishi, Japan).

A centrifugal suction fan 1 HP with air flow rate 30 cmm/m² [12] was used for sucking the exhaust drying air. An anemometer (Velocicalc-Plus, TSI, USA) was used to measure the drying air velocity.

The jet burner using kerosene (OL-3, Daewon, Korea) was used for heating drying air. The burner can be raised to the temperature of drying air up to 140°C. A temperature sensor (PT-100 Ω) was installed at the influx duct to control the burner, and a temperature control equipment (HSD-V2, Hansung, Korea) was used. An electric balance (A-200, Cass, Korea, accuracy 0.01 kg) was used to weigh the mass of Kerosene loss by drying process.

The dimension of drying chamber (height × length × width) is 0.5 m × 0.7 m × 0.5 m. Height of tempering section is 0.5 m. In both experiments, rapeseed samples using are Spring rapeseed, variety Sunmang F1-hybrid, were harvested in June in Jeonnam-do, Yeonggwang-gun. The samples of 200 kg were cleaned and stored in a refrigerator at a temperature of 4°C [13]. The initial moisture content of samples in Test 1 is 23.0% and in Test 2 is 23.2% (**Table 3**).

4.3 Experimental results

In both experiments, there are a difference in drying air temperature in the plenum chamber. The drying air temperature is highest at the position in front of the plenum, and lowest at back of plenum. In Test 1, the average temperature of drying air in the plenum section is 96.9, 84.2, and 83.9°C at the front, middle, and back of the plenum, respectively. In Test 2, the average temperature of drying air in plenum section is 128.1, 111.3, and 106.1°C at front, middle, and back of plenum, respectively (**Table 4**). The average temperature of drying air in the plenum chamber during drying process is 89.4 and 116.8°C for Test 1 and Test 2, respectively (**Figure 8**).

The temperature of rapeseed during drying at discharge augers (**Figure 9**) and the temperature of air at exhaust ducts (**Figure 10**) for both Test 1 and Test 2 are fairly uniform. Detailed drying conditions in Test 1 and Test 2 shown in **Table 5** and results of rapeseed drying in a pilot-scale dryer were summarized in **Table 6**.

Rapeseed	Test 1	Test 2
Initial weight (kg)	200	200
Initial moisture content (% w.b.)	23.0	23.2
Initial grain temperature (°C)	22.8	24.7

Table 3.
Initial rapeseed conditions.

Test no.	Drying air temperature (°C)		
	Front	Middle	Back
Test 1	96.9	84.2	83.9
Test 2	128.1	111.3	106.1

Table 4.
Drying air temperature in the plenum chamber.

After the experiment was completed, dried rapeseed samples were sealed in double-layer polythene bags for 24 h to reach ambient conditions [14]. The samples were then tested for germination. The germination tests were conducted according

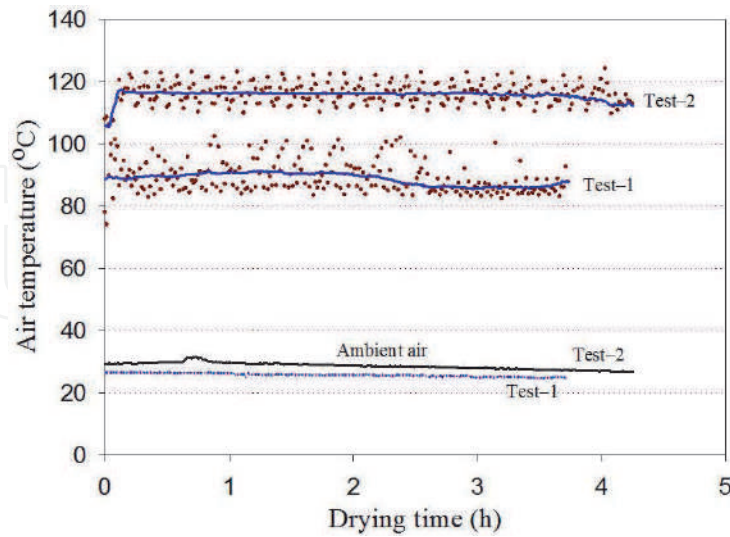


Figure 8.
Average variation of drying air temperature during drying process.

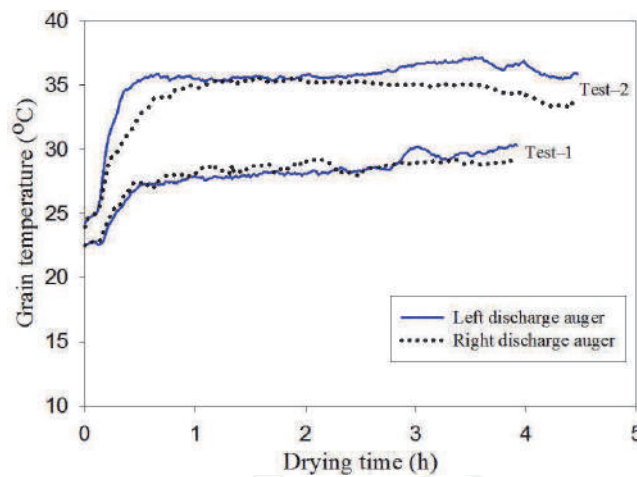


Figure 9.
Rapeseed temperature during drying process at discharge augers.

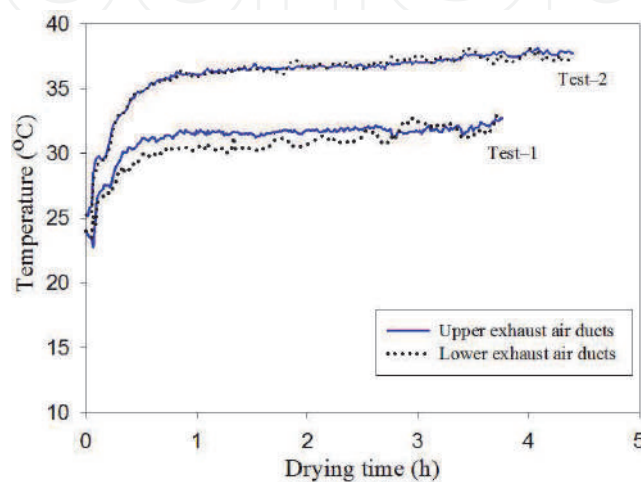


Figure 10.
Temperature of exhaust drying air in test 1 and test 2.

to protocols described for the standard germination test [15]. The average germination percentages of Test 1 and Test 2 are 94.7 and 84.5%, respectively [16].

4.4 Model validation

The simulation program was validated by comparison results of numerical model with experimental data of pilot-scale concurrent-flow dryer as described. The input data of simulation program were entered in accordance with the data of the actual experiment, such as initial rapeseed conditions, dryer specification, and drying air and ambient air conditions. The fitness of simulated results with measured results was evaluated based on the coefficient of determination (R^2) and the root mean square error (RMSE).

The R^2 of moisture content versus drying time in Test 1 and Test 2 were 0.994 and 0.997, respectively. The RMSE of moisture content in Test 1 and Test 2 were 0.334 and 0.506%w.b., respectively. The comparison of the measured and

Test No.	Average drying air temperature (°C)	Air flow rate (cmm/m ²)	Ambient air temperature (°C) Ave. (min-max)	Ambient relative humidity (%) Ave. (min-max)
Test 1	89.4	30	25.4 (24.2–26.4)	71.6 (67.1–75.3)
Test 2	116.8	25	28.6 (26.7–31.4)	63.4 (60.8–68.0)

Table 5.
Drying conditions for drying tests.

Experimental results	Test 1	Test 2
Initial moisture content (% w.b.)	23.0	23.2
Final moisture content (% w.b.)	13.8	11.4
Drying time (h)	3.90	4.22
Drying rate (% w.b./h)	2.38	2.80
Fuel consumption (kJ/kg-water)	4915	4831
Initial germination rate (%)	94.7	84.5

Table 6.
The results of rapeseed drying in pilot-scale dryer.

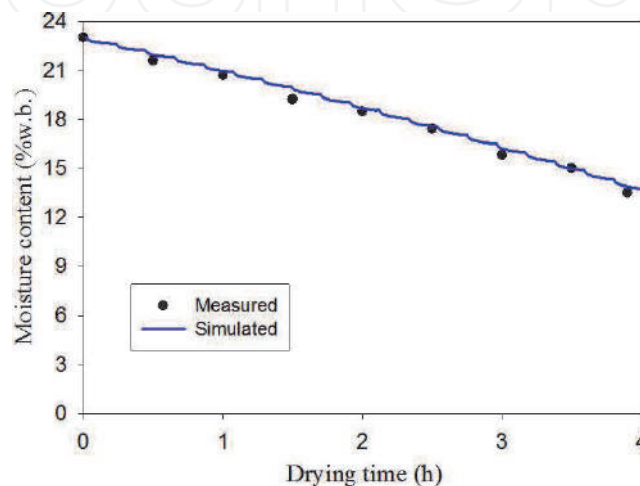


Figure 11.
Measured and simulated moisture content in test 1.

simulated moisture content during drying process for Test 1 is shown in **Figure 11** and for Test 2 shown in **Figure 12**.

The analytical results showed the good fitness between simulated moisture content and measured moisture content for both Test 1 and Test 2. This result showed the good agreement of the simulation program for predicting the moisture content of rapeseed in concurrent-flow dryer.

The simulated temperature of rapeseed during drying process has a good correlative with the experimental data. The R^2 of rapeseed temperature are 0.904 and 0.925 in Test 1 and Test 2, respectively. The RMSE of rapeseed temperature are 1.15 and 1.77°C in Test 1 and Test 2, respectively. The comparison of the measured and simulated temperature of rapeseed for Test 1 is shown in **Figure 13** and for Test 2 shown in **Figure 14**. The analytical results showed that simulated values have a very good fitness to measured values by experiment.

The discharge rapeseed temperature of the simulation program tends to be higher than the measured values during drying process. However, the average differences between measured and simulated values are small. It showed a good fitness between the values of the model and the values of the experiments.

The drying time, drying rate, fuel energy consumption, and germination ratio of rapeseed after drying were investigated. The comparison of the measured and simulated results of both Test 1 and Test 2 was listed in **Table 7**.

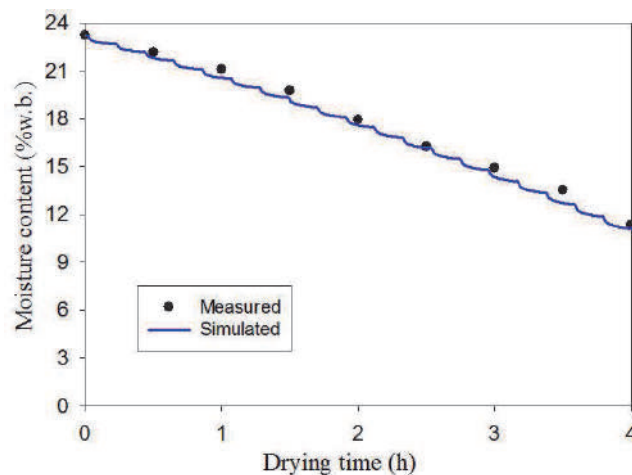


Figure 12.
Measured and simulated moisture content in test 2.

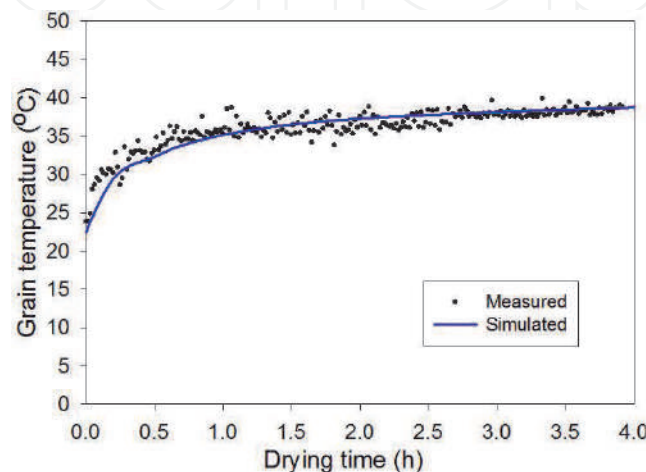


Figure 13.
Measured and simulated temperature of rapeseed in test 1.

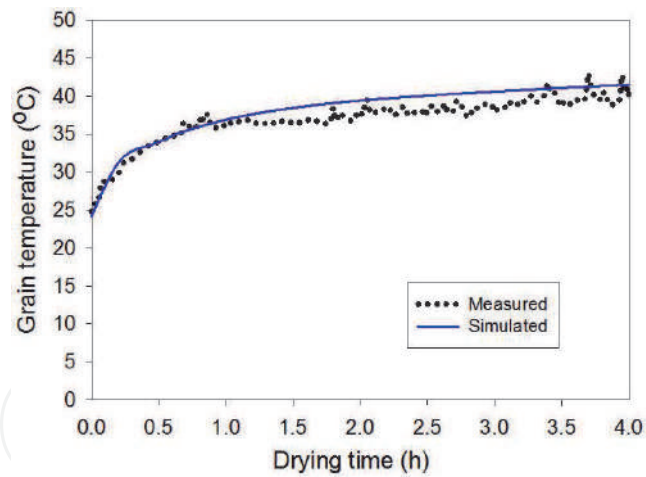


Figure 14.
Measured and simulated temperature of rapeseed in test 2.

Test 1	Measured	Simulated	Difference (%)
Final moisture content (% w.b.)	13.8	13.5	2.2
Drying rate (% w.b./h)	2.38	2.26	5.04
Fuel energy (kJ/kg-water)	4915	5153	4.62
Drying time (h)	3.9	4.2	7.14
Germination ratio (%)	94.7	96.5	1.87
Test 2	Measured	Simulated	Difference (%)
Final moisture content (% w.b.)	11.4	10.8	5.17
Drying rate (% w.b./h)	2.80	2.95	5.08
Fuel energy (kJ/kg-water)	4831	4417	8.57
Drying time (h)	4.22	4.2	0.47
Germination ratio (%)	84.5	92.5	8.64

Table 7.
Measured and simulated results of test 1 and test 2.

The difference between measured value and simulated value of final moisture content were 2.2 and 5.17%; drying rate were 5.04 and 5.08%; drying time were 7.14 and 0.47%; and germination ratio were 1.87 and 0.47%. The simulated values of fuel energy consumption for drying were 4.62 and 8.57% lower than the measured values for Test 1 and Test 2, respectively. The differences are derived from the sequential changes in drying air temperature, ambient temperature, and drying air humidity of the simulation model and experiment conditions. In general, there is a good fitness between measured values by experiment and simulated values from the simulation program for all of the output parameters such as final moisture content, drying time, drying rate, fuel energy, and germination ratio at the different experiment conditions.

5. Conclusions

Mathematical modeling for rapeseed drying on concurrent-flow dryer was built based on energy and mass transfer balances applied for both fluid and solid phases

of a concurrent-flow dryer. Energy balances and mass balances are written on a differential volume located at an arbitrary location in the grain bed. The mathematical model consists of a set of four partial differential equations in four independent variables including air humidity, air temperature, grain temperature, and grain moisture content.

A computer simulation program for circulating concurrent-flow rapeseed dryer was developed using these models along with a detailed description of the program. The simulation program can predict the drying time, drying rate, drying air humidity and temperature, grain temperature and moisture content during drying process, water removal rate, drying fan parameters, germination ratio, fuel energy, and total energy consumption.

To evaluate a fitness of simulation program, a pilot-scale concurrent-flow dryer with a capacity of 200 kg/batch was designed, manufactured, and tested. Two drying experiments were conducted. The output parameters of the simulation program were compared and analyzed with experiment data.

The RMSE of simulated moisture contents ranged from 0.334 to 0.506%w.b. with the coefficient of determinations ranging from 0.994 to 0.997. The RMSE of simulated rapeseed temperatures ranged from 1.15 to 1.77°C with the coefficient of determinations ranging from 0.904 to 0.925. The experimental drying rates were 2.38 and 2.80% w.b./h. The difference between simulated value and measured value of drying rate were 5.04 and 5.08%; drying time were 7.14 and 0.47%; and germination ratio were 1.87 and 0.47%. The simulated fuel energy consumption for drying were 4.62 and 8.57% lower than the experimental values.

The analytic results showed that the simulation results have good fitness with experimental data. So, the mathematical modeling and the simulation program were proved their reliability and were shown to be a convenient tool for simulation of rapeseed drying in circulating concurrent-flow dryer.

Author details

Le Anh Duc^{1*} and Keum Dong Hyuk²

¹ Nong Lam University, Ho Chi Minh City, Vietnam

² SungKyunKwan University, Suwon, South Korea

*Address all correspondence to: leanhduc@hcmuaf.edu.vn

IntechOpen

© 2020 The Author(s). Licensee IntechOpen. This chapter is distributed under the terms of the Creative Commons Attribution License (<http://creativecommons.org/licenses/by/3.0>), which permits unrestricted use, distribution, and reproduction in any medium, provided the original work is properly cited. 

References

- [1] Thompson TL, Peart RM, Foster GH. Mathematical simulation of corn drying—a new model. *Transactions of ASAE*. 1968;**24**(3):582-586
- [2] Felipe CAS, Barrozo MAS. Drying of soybean seeds in a concurrent moving bed: Heat and mass transfer and quality analysis. *Drying Technology*. 2003; **21**(3):439-456
- [3] Keum DH, Han JG, Kang SR, Kim OW, Kim H, Han JW, et al. Development of rice circulating concurrent-flow dryer (I) - performance test of pilot scale dryer. *Journal of Biosystems Engineering*. 2005;**10**(2):97-106
- [4] Han JW, Keum DH, Kim W, Duc LA, Cho SH, Kim H. Circulating concurrent-flow drying simulation of rapeseed. *Journal of Biosystems Engineering*. 2010;**35**(6):401-407
- [5] Keum DH. *Simulation of Agricultural Products and Foods Process Engineering*. South Korea: SungKyunkwan University Publisher; 2005
- [6] Duc LA, Han JW, Hong SJ, Choi HS, Kim YH, Keum DH. Physical properties of rapeseed (I). *Journal of Biosystems Engineering*. 2008;**33**(2):101-105
- [7] Gallaher GL. A method of determining the latent heat of agricultural crops. *Agricultural Engineering*. 1951;**32**(1):34-38
- [8] Duc LA, Hyuk KD. Equilibrium moisture content isotherm characteristics of rapeseed. *Asia Pacific Journal of Sustainable Agriculture, Food and Energy*. 2016;**4**(1):10-14
- [9] Cenkowski S, Muir WE, Jayas DS. Simulation of canola and barley drying in deep bed. *Journal of Food Process Engineering*. 1989;**12**:171-190
- [10] Duc LA, Han JW, Keum DH. Thin layer drying characteristics of rapeseed (*Brassica napus* L.). *Journal of Stored Products Research*. 2011;**47**(1):32-38
- [11] Fausett LV. *Applied Numerical Analysis Using Matlab*. Upper Saddle River, New Jersey: Prentice Hall Inc.; 1999. p. 07458
- [12] Hong SJ, Duc LA, Han JW, Kim H, Kim YH, Keum DH. Physical properties of rapeseed (II). *Journal of Biosystems Engineering*. 2008;**33**(3):173-178
- [13] Cassells JA, Caddick LP, Green JR, Reuss R. Isotherms for Australian canola varieties. In: *Proceedings of the Australian Postharvest Technical Conference*. 2003. pp. 59-63
- [14] ANSI/ASAE S448.1. Thin-layer drying of agricultural crops. In: *ASAE Standards 51st Edition*. 2004. pp. 598-600
- [15] Association of Official Seed Analysis. Rules for testing seeds. *Journal of Seed Technology*. 1993;**16**:1-113
- [16] Duc LA, Han JW. The effects of drying conditions on the germination properties of rapeseed. *Journal of Biosystems Engineering*. 2009;**34**(1):30-36

Determination on Fluidization Velocity Types of the Continuous Refined Salt Fluidized Bed Drying

Bui Trung Thanh and Le Anh Duc

Abstract

After the centrifugation stage, refined salt particles have rather high moisture content; therefore, the moist salt particles in contact with each other will stick together in a short time. In particular, the moist salt particles will stick together faster and tighter and form a larger unit when they are exposed to drying hot air. For this reason, the refined salt was dried by rotary drum dryers with vibrating balls distributed along the drum or a vibrating fluidized bed dryers. These drying methods make poor product sensory quality, low product recovery efficiency, while also lead to an increase of heat and electricity energy consumption. In order to increase the efficiency of refined salt drying technology by conventional continuous fluidized bed dryers, the chapter focuses on the study of aerodynamic properties of refined salt grains in the continuous fluidized particle layer. The content of the chapter presents theoretical and empirical methods to determine fluidization velocity types in designing a continuous fluidized bed dryer.

Keywords: refined salt, solid particles, aerodynamic, minimum fluidization velocity, homogeneous fluidization, bed fraction, fluidized bed dryer

1. Introduction

1.1 Preface

The phenomenon in which solid particles float in a gas stream and have a liquid-like property is called a fluidized bed. This phenomenon of fluidization in gas or liquid flow was discovered by Fritz Winkler in the 1920s [1]. This one was investigated by Lewis et al. and had been raised to fluidized theory [2]. The first commercial fluidized bed dryer was installed in USA in 1948 [3]. The fluidized bed technology is used for drying of bulk materials, includes examples such as: vibrating fluidized bed dryer, normal fluidized bed dryer without vibrating device and pulsed fluidized bed dryer.

Mathematical modeling and computer simulation of grain drying are now widely used and become an important tool for designing new dryers, for analyzing existing drying systems and for identifying drying conditions [4]. Identifying the drying conditions is necessary to establish the optimal protocol for ensuring seed quality [5]. To solve the simulation models, equations concerning aerodynamic properties such as the gas stream velocity and particle velocity are the most important components. The aerodynamic properties are affected by shape, density and size of particles [6].

Order	Function of gases	Function of solid materials	Equipment in practice
1	Heat carrier	Materials do not react to gases	<ul style="list-style-type: none"> • Heaters supply to materials • Heat exchangers with heat recovery
2	Loading and transportation of particle materials	Materials do not react to gases	Pneumatic solid particle carrier
3	Heat carrier and material loading and transportation	Materials do not react to gases	Aerodynamic dryers
4	Chemical agents	<ul style="list-style-type: none"> • Chemical reaction • Activated material for chemical reactions • As inert material which is used in fluidized bed combustion of boiler 	<ul style="list-style-type: none"> • The burner burns • Gasification equipment • Catalytic reconstitution • Oxidation equipment • Processing of metallurgical surfaces and annealing furnace
5	Agitation	Materials do not react to gases	Mixer of different materials in the tank

Table 1.

Relations and functions of gas interacting with solid particle in real production.

In recent years, the fluidized bed technology has been concerned in the application in the sugar drying and refined salt drying in Vietnam. In the scope of this chapter, we discuss the issues related to the hydrodynamics of refined salt particles in the gas stream at ambient temperature and temperature equivalent to that of drying particle. The focus of this chapter is to determine the velocity values of the gas through the particle layer to form the minimum, homogeneous and critical fluidized layers.

In industrial manufacturing practice, we often encounter the contact, interaction between solid-particle materials and gases. These interaction phenomena are described in **Table 1**.

1.2 Applied materials in fluidized bed drying technology

According to Abrahamsen and Geldart [7], the two most important factors affecting the fluidization characteristic of the particle layer are particle size and particle density.

Geldart [8] visually observed the various conditions and classified fluidizable particles into four groups: A, B, C and D. As a result, the classification was related to the influence of the average particle size and particle density on the properties of the fluidized layer, as depicted in **Figure 1** and **Table 2**.

According to the content of this chapter, we focus on approaching, researching and experimenting on the mechanism and principle of interaction between air and the applied material in fluidized bed drying. The approach method is to arrange a stream of heat-carrying air blowing from the bottom of the particle chamber through a gas distributor (the holes arranged at an angle to the cross section of the tank). Hot air stream is evenly distributed and touches the surface of particles in tank (the particle layer was on the gas distributor). The continuous air stream ensures that the contact of particle surfaces with the gas flow is consecutive. The nature of the gas flowing through the particle layer may be laminar, turbulent, or transition flow at the material contact surface. The inflow of hot air affects the velocity of the interaction between the gas stream and the material.

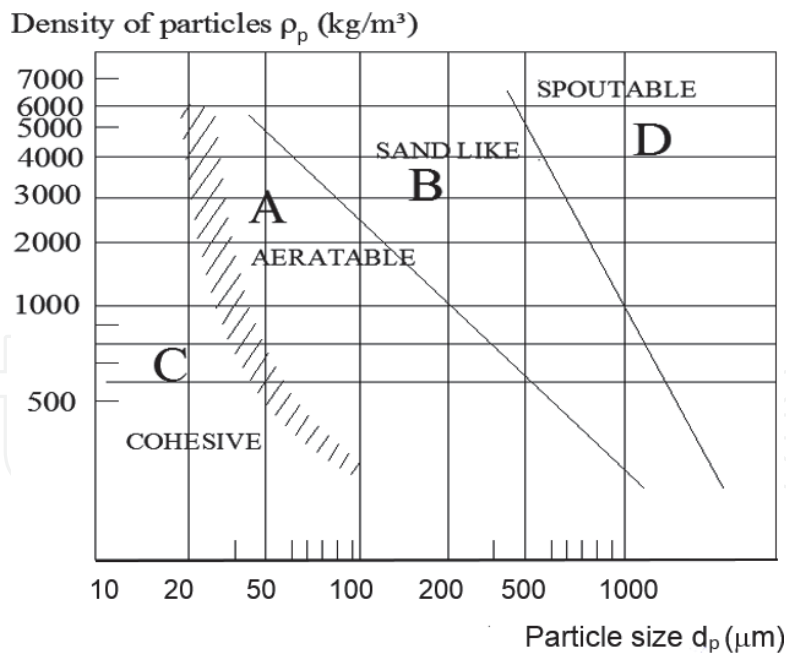


Figure 1.
 Diagram of the Geldart classification of particles [9, 10].

1.3 Basic concept of fluidized particle layer and principle of fluidized particle layer creation

When the material layer is fluidized, its state is converted from a fixed bed to a dynamic state. The particle layer has liquid-like properties. The surface area of the particles contacting with the fluid increases, and therefore the heat transfer ability from fluid to particles rapidly rises.

In order for the fluidization phenomena to occur in the bulk material layer, the air stream must have sufficient pressure and velocity. The air stream flows upward, passes through the particle materials (follow the linear increment) through uncountable air holes of the distributor, which are arranged at the bottom of the particle material layer. When the velocity of air stream is small, pressure exerted on particles is small, the particle layer maintains its original fixed bed (the state from 0 before point A, **Figure 2**). As the air velocity is increased further, the aerodynamic traction appears, which has opposite effect of the gravitational force of the particles, causing the expansion of particle layers in a volume, and the particles begin to move apart from each other (at point A, **Figure 1**).

By further raising the velocity of air stream to the critical value, the friction force between the particles and air is equal to the weight of particles. At this time, the vertical component of the compression pressure is eliminated, the upward-pulling force equals the downward gravity, causing the particle material to be suspended in the air stream. When the gas velocity reaches the critical value, the particle material layer will be converted to complete fluidization state, called the fluidization particle layer and having the liquid-like properties (position from A to B in **Figure 2**).

By further increasing the velocity of the gas, the bulk density of the particle layers continues to decrease, its fluidization becomes more violent, until the particles no longer form a bed and are swept up and fallen down in the fluidization motion (position from B to C, **Figure 2**). At this time, each particle material is covered with gas flow, the intensity of the heat and material transfer occurs violently. When granular material is fully fluidized, the bed will conform to the volume of the chamber, its surface remaining perpendicular to gravity; objects with a lower

Particle group characteristics	C group	A group	B group	D group
Particle size (μm)	0–3	$30 \leq d_p \leq 100$	$100 \leq d_p \leq 1000$	≥ 1000
Density (kg/m^3)	Smallest	1400	400–4500	Lower than other materials
The most obvious characteristics of group	<ul style="list-style-type: none"> • Particles are cohesive and linked • Difficult fluidization 	<ul style="list-style-type: none"> • Easy fluidization • Dense phase expands stably before bubbling starts 	<ul style="list-style-type: none"> • Starting on bubble creation at the minimum fluidized velocity value 	<ul style="list-style-type: none"> • The rough solid particles
Typical granulars	<ul style="list-style-type: none"> • Flour • Cement 	<ul style="list-style-type: none"> • Milk flour • FCC granular 	<ul style="list-style-type: none"> • Construction sands 	<ul style="list-style-type: none"> • Pebbles in rice • Coffee beans, wheat, lead shot
Properties of fluidization layer				
Particle layer expansion	<ul style="list-style-type: none"> • Channeling possibilities in the particles layer easily 	<ul style="list-style-type: none"> • The large bed expansion before bubbling is started • The minimum fluidization velocity is smaller than minimum bubbling 	Medium	Difficult to fluidize evenly (low)
Properties of air bubbles	<ul style="list-style-type: none"> • Do not form bubble 	<ul style="list-style-type: none"> • It does not form bubble fluidization • There is a maximum bubble size 	<ul style="list-style-type: none"> • The bubbles rise faster than the interstitial gas • Bubbles are large and grow rapidly and coalesce, as they rise through the bed 	<ul style="list-style-type: none"> • Bubbles rise more slowly than the rest of the gas percolating through the emulsion
Property of mixed solid particles	Very low	High	Solids' recirculation rates are smaller	Low
Spaying	None	None	Only occurs in the upper layer	<ul style="list-style-type: none"> • It occurs • Only occur in under layers

Table 2. *The classification of fluidization properties of particle groups according to Geldart [9, 11].*

density than the bed density will float on its surface, bobbing up and down, while objects with a higher density sink to the bottom of the bed.

Fluidization has many applications in many technologies of manufacturing practice, such as mixing different types of granular materials; fluidized bed drying; cooling grain after drying; supporting interaction between chemicals in the fluidized bed; granulation technology; film coating technology of medicine and pharmacy; manufacturing technology through the combined use of organic and inorganic fertilizers; and biomass fuel combustion technology in fluidized bed.

To clarify the dynamics of the fluidized beds for application in refined salt drying in the fluidized bed, the theoretical and experimental issues determining the velocity of gas through the particle layers to form different fluidized layers are described as follows.

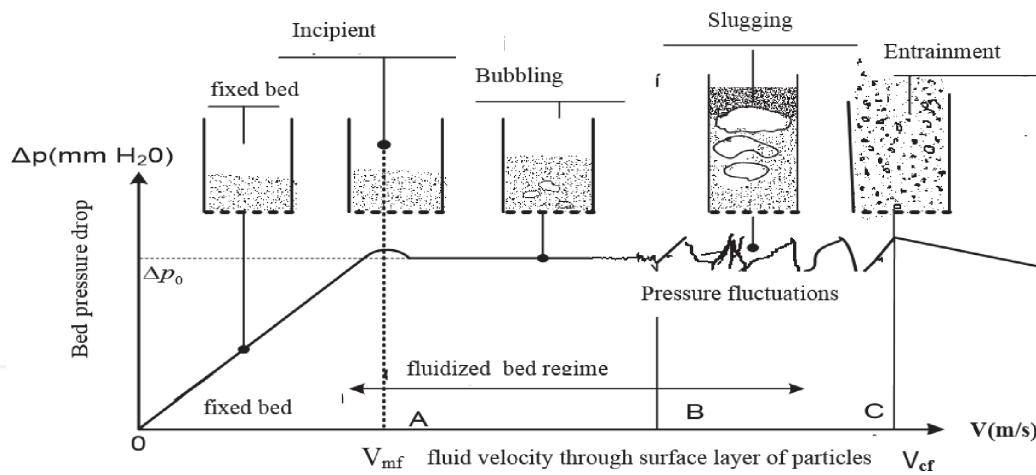


Figure 2.
 Particle layer states with gas velocity changing [10].

2. Methodology

2.1 Determination of the minimum fluidization velocity from publications

2.1.1 Determination of V_{mf} using the Ergun equation

When the air stream having sufficient pressure and velocity passes through the static spherical particle layers, they begin to expand (the particles become “flexible”). In this condition, it is called the minimum particulate fluidization state and is described by the modified equation of Ergun (see position A in **Figure 1**) [12].

$$\frac{\Delta P}{H_{mf}} = \frac{150\mu_f(1 - \epsilon_{mf})^2 V_{mf}}{\epsilon_{mf}^3 d_p^2} + \frac{1.75(1 - \epsilon_{mf})\rho_f V_{mf}^2}{\epsilon_{mf}^3 d_p} \quad (1)$$

For particles of arbitrary shapes, the pressure drop of air stream at the minimum fluidization state is represented by Eq. (2). The spherical value of particle material got in the Eq. (1) [10] is given by:

$$\frac{\Delta p}{H_{mf}} = 150 \frac{(1 - \epsilon_{mf})^2}{\epsilon_{mf}^3} \frac{\mu_f V_{mf}}{(\phi d_m)^2} + 1.75 \frac{(1 - \epsilon_{mf})}{\epsilon_{mf}^3} \frac{\rho_f V_{mf}^2}{\phi d_m} \quad (2)$$

For the particle layer to be converted from a fixed state to a fluidization state, the pressure of air stream must be large enough to overcome the weight of the particle layers and it is determined by Eq. (3) [10].

$$\Delta p = \frac{m}{\rho_p A} (\rho_p - \rho_f) g \quad (3)$$

In Eq. (3), it is considered that there was no interaction force between particles in layer and no interaction between particles and the wall of the tank. So, that did not cause the pressure increasing effect. Thus, the pressure drop of the air stream was constant while increasing the gas velocity from the smallest fluidization velocity to the value when the entrainment process of particles occurred (position C, **Figure 2**).

In Eqs. (1) and (2), it is also shown that the pressure drop of the gas stream that is generated through the fluidized particle layer is depended on the particle size (d_p), the bed voidage (ϵ) and the gas temperature (t °C). According to Eq. (3), the

pressure drop of the gas stream through the particle layers is dependent upon the material mass (m), the gas distributor grate area (A), particle density (ρ_p) and gas density (ρ_f). Thus, we could calculate the minimum fluidization velocity value (V_{mf}), which was based on Eqs. (1)–(3) for non-spherical particles by solving Eq. (4).

$$\frac{m \cdot H_{mf}}{\rho_p \cdot A} (\rho_p - \rho_f) g = 150 \frac{(1 - \varepsilon_{mf}) \mu_f V_{mf}}{\varepsilon_{mf}^3 (\phi d_p)^2} + 1.75 \frac{\rho_f V_{mf}^2}{\varepsilon_{mf}^3 \phi d_p} \quad (4)$$

The minimum fluidization velocity (V_{mf}) is the root of Eq. (4), which is based on available parameters, such as the height of minimum fluidization bed (H_{mf}), the mass of particles in the air distributor (m), the area for gas distribution or called cross-sectional area of the bed (A), particle density (ρ_p), air density (ρ_f), mean particle diameter (d_p), spherical degree of particles (ϕ) and void fraction at minimum fluidization particle layer (ε_{mf}).

Commonly, the sphere degree of particles (ϕ) must be determined in experiments [10]. The spherical degree of refined salt particles was found out by Bui [13–15]. Theoretically, in order to fluidize the particle layer, the actual weight of the solid particles must be equal to the force exerted on the particle layers and that is equal to the pressure drop across the bed (ΔP) multiplied by the cross-sectional area of the chamber (A). A minimum fluidization layer which must have determined layer thickness (H_{mf}), void fraction (ε_{mf}), then the expanded volume of the fluidized particles (U) has the value of the Eq. (5):

$$U = (1 - \varepsilon_{mf}) \cdot A \cdot H_{mf} \quad (5)$$

And the actual gravity of the particle mass has a value of:

$$W = (1 - \varepsilon_{mf}) (\rho_p - \rho_f) \cdot A \cdot H_{mf} \cdot g \quad (6)$$

The balance of the real gravity components of the particle mass and the upward force exerted on the particle mass of the gas flow was calculated according to

$$\Delta P = (1 - \varepsilon_{mf}) (\rho_p - \rho_f) \cdot H \cdot g \quad (7)$$

Substituting Eq. (8) into Eq. (1) or Eq. (2) yields Eq. (9).

$$(1 - \varepsilon_{mf}) (\rho_p - \rho_f) \cdot H_{mf} \cdot g = 150 \frac{(1 - \varepsilon_{mf})^2 \mu_f V_{mf}}{\varepsilon_{mf}^3 (\phi d_p)^2} + 1.75 \frac{(1 - \varepsilon_{mf}) \rho_f V_{mf}^2}{\varepsilon_{mf}^3 \phi d_p} \quad (8)$$

$$150 \frac{(1 - \varepsilon_{mf})}{\phi^2 \varepsilon_{mf}^3} \text{Re}_{mf} + \frac{1.75}{\phi \varepsilon_{mf}^3} \text{Re}_{mf}^2 = Ar \quad (9)$$

Giving physical parameters of particle and gas into the Eq. (8), velocity (V_{mf}) was found out. In case of very small particles, the gas stream regime through the particle layer was laminar flow and the minimum fluidization velocity should be calculated by the Ergun equation [12]. In case of $\text{Re}_{mf} < 1$, we use Eq. (9) to calculate the minimum fluidization velocity of gas.

2.1.2 Determination of V_{mf} by the correlation of Re_{mf} and Archimeter (Ar)

When gas passes through the particle bulk, which can have any shape, the minimum fluidization Reynolds coefficient (Re_{mf}) is determined by Eq. (10).

$$\text{Re}_{mf} = \frac{\rho_{mf} \cdot V_{mf} \cdot d_p \cdot \phi}{\mu_f} \quad (10)$$

Eq. (11) describes the correlation between Ar and Re_{mf} with void fraction at minimum fluidization particle layer (V_{mf})

$$\text{Ar} = 150 \frac{(1 - \varepsilon_{mf})}{\phi^2 \varepsilon_{mf}^3} \text{Re}_{mf} + \frac{1.75}{\phi \varepsilon_{mf}^3} \text{Re}_{mf}^2 \quad (11)$$

Archimeter (Ar) is determined by Eq. (12) for particles of any shape.

$$\text{Ar} = \frac{\rho_f (\rho_p - \rho_f) g (\phi d_p)^3}{\mu_f^2} \quad (12)$$

Set up Eq. (13):

$$\frac{\rho_f (\rho_p - \rho_f) g (\phi d_p)^3}{\mu_f^2} = 150 \frac{(1 - \varepsilon_{mf})}{\phi^2 \varepsilon_{mf}^3} \text{Re}_{mf} + \frac{1.75}{\phi \varepsilon_{mf}^3} \text{Re}_{mf}^2 \quad (13)$$

Substituting physical parameters into the Eq. (12), which includes the particle density (ρ_p), the gas density at the temperature of minimum fluidization velocity (ρ_f), the air dynamic viscosity (μ_f), spherical degree of particle (ϕ), void fraction at the minimum fluidization velocity (ε_{mf}), mean particle diameter (d_m) [13–15] and getting Ar number value into the Eq. (13). Then, we solved the quadratic equation to find out the root of equation Re_{mf} in Eq. (10), we got only the positive value. Thus, we calculated the minimum fluidization velocity (V_{mf}) from Eq. (10).

2.1.3 Determination of V_{mf} by the Kozeny-Carman correlation

Kozeny-Carman gave the formula of calculation of the minimum fluidization velocity for a very small particle size with the $\text{Re}_{mf} < 10$ in Eq. (14) described in Yates [16].

$$V_{mf} = \frac{g (\rho_p - \rho_f)}{150 \mu_f} \frac{\varepsilon_{mf}^3}{1 - \varepsilon_{mf}} \phi^2 d_p^2 \quad (14)$$

For spherical particles or sphericity equivalent, the bed voidage of the minimum fluidization $\varepsilon_{mf} = 0.4 \div 0.45$.

2.1.4 Determination of V_{mf} by correlation of Wen and Yu

In case of the unavailability of the sphericity of particles, we determine the minimum fluidization velocity (V_{mf}) by using of the experimental correlation of Wen and Yu [17]. An empirical formula of calculation of the void fraction at minimum fluidization particle layers in Eq. (15) or Eq. (16) with the available sphericity degree of particle (ϕ) or the calculation of the sphericity degree of particle (ϕ) in case void fraction (ε_{mf}) at minimum fluidization particle layer is available, which was also described by Wen and Yu equation (cited in Howard, 1989) [10].

$$\frac{1 - \varepsilon_{mf}}{\phi^2 \varepsilon_{mf}^3} \approx 11 \text{ or } \frac{1}{\phi \varepsilon_{mf}^3} \approx 14 \quad (15)$$

We can use the calculation of the void fraction at minimum fluidization particle layers from the other correlation, which is also converted from Wen and Yu.

$$\varepsilon_{mf} = \left(\frac{0.071}{\phi} \right)^{1/3} \quad (16)$$

It is based on the calculation of the void fraction (ε_{mf}) (at position A in **Figure 2**) of Eq. (15) or Eq. (16) and substituting the obtained ε_{mf} value into the Ergun Eq. (2), we have Eq. (17).

$$Ar = 1650 \text{ Re}_{pmf} + 24.5 \text{ Re}_{pmf}^2 \quad (17)$$

Using the calculated Ar number from Eq. (12) and substituting the Ar value into Eq. (17), we obtain Eq. (18) to calculate the particle Reynolds number at the minimum fluidization velocity (Re_{mf}).

$$\text{Re}_{mf} = \frac{-1650 \pm \{1650 + (4 \times 24.5 Ar)\}^{1/2}}{2 \times 24.5} \quad (18)$$

Taking the positive square root, we get Eq. (19):

$$\text{Re}_{mf} = (33.7^2 + 0.0408 Ar)^{1/2} - 33.7 \quad (19)$$

It was applied to calculate for solid particles with size larger than 100 μm [10]. From the Re_{mf} value that was found out in the Eq. (19), V_{mf} is calculated according to Eq. (10). In case of solid particles with small size (C group of Geldart, 1973) in the specified temperature conditions, the V_{mf} value is calculated in Eq. (20) by Wen and Yu.

$$V_{mf} = 7.90 \cdot 10^{-3} d_p^{1.82} (\rho_p - \rho_f) 0.94 \mu_f^{-0.83} \quad (20)$$

2.1.5 Determination of V_{mf} by the correlation of Beayens and Geldart

For solid spherical particles with diameters ranging from 0.05 to 4 mm ($0.05 \text{ mm} < d_p < 4 \text{ mm}$) and particle density ranging from 850 to 8810 kg/m^3 ($850 \text{ kg/m}^3 < \rho_p < 8810 \text{ kg/m}^3$), the method of calculation of V_{mf} was proposed by Beayens and Geldart as shown in Eq. (21) [18].

$$Ar = 1823 \text{ Re}_{mf}^{1.07} + 21.7 \text{ Re}_{mf}^2 \quad (21)$$

Then the V_{mf} can be calculated from Eq. (22) in case of available solid particle and gas parameters.

$$V_{mf} = \frac{9.125 \times 10^{-4} \left((\rho_p - \rho_f) g \right)^{0.934} d_p^{1.8}}{\mu_f^{0.87} \rho_p^{0.66}} \quad (22)$$

2.1.6 Determination of V_{mf} by correlation of Goroshko

The minimum fluidization velocity of spherical particles was determined by correlation shown in Eq. (23) by Goroshko described in Howard [10, 19].

$$a \operatorname{Re}_{mf}^2 + b \operatorname{Re}_{mf} - Ar = 0 \quad (23)$$

where

$$a = \frac{1.75}{\phi \varepsilon_{mf}^3} \text{ and } b = \frac{150(1 - \varepsilon_{mf})}{\phi^2 \varepsilon_{mf}^3} \quad (24)$$

We get ϕ is 1.0 ($\phi = 1$) then solving the Eq. (23) take the spherical degree value, we have the Eq. (25).

$$\operatorname{Re}_{mf} = \frac{-b + (b^2 + 4aAr)^{1/2}}{2a} \quad (25)$$

Multiplying $(b + \sqrt{b^2 + 4aAr})$ by the numerator and denominator of Eq. (25), we have the Eq. (26)

$$\operatorname{Re}_{mf} = Ar \left\{ \frac{b}{2} + \left[\left(\frac{b}{2} \right)^2 + aAr \right]^{1/2} \right\}^{-1} \quad (26)$$

And its value was determined by Eq. (27) by Goroshko:

$$\operatorname{Re}_{pmf} = \frac{Ar}{b + \sqrt{aAr}} \quad (27)$$

Eq. (27) is different from Eq. (26) by the added value $(\frac{b}{2})^2 + aAr = \frac{b}{2} + \sqrt{aAr}$. There is a difference in Re_{mf} value between the Goroshko equation and Ergun equation. The Re_{pmf} of Goroshko equation [Eq. (27)] is smaller than Re_{mf} of Ergun [Eq. (26)]. This deviation interval depends on the value of Archimedes (Ar). Thus, we have a correlation equation, which is described in Eq. (28).

$$\frac{\operatorname{Re}_{mf}(\text{Ergun})}{\operatorname{Re}_{pmf}(\text{Goroshko})} = \frac{b + \sqrt{aAr}}{\left\{ \frac{b}{2} + \left[\left(\frac{b}{2} \right)^2 + aAr \right]^{1/2} \right\}} \quad (28)$$

2.1.7 Determination of V_{mf} following Goroshko and Todes equation

The minimum fluidization velocity (V_{mf}) of sphericity particles was defined from the Re_{mf} by Goroshko et al. in Eq. (29) [19].

$$\operatorname{Re}_{pmf} = \frac{Ar}{150 \frac{1 - \varepsilon_{mf}}{\varepsilon_{mf}^3} + \sqrt{\frac{1.75}{\varepsilon_{mf}^3} Ar}} \quad (29)$$

In case of non-spherical particles with different sizes, the Re_{pmf} value was error from 15–20% in case we use the Eq. (29) of calculation described in [20]. In the case of rapid calculation, we considered the bed voidage of the minimum fluidization state to be equal to the bed voidage at static particle layers ($\varepsilon_o = \varepsilon_{mf} = 0.4$), and the Re_{mf} is calculated in Eq. (30) [21].

$$\operatorname{Re}_{mf} = \frac{Ar}{1400 + 5.22\sqrt{Ar}} \quad (30)$$

2.1.8 Determination of V_{mf} following Leva

From the formula of Carman-Kozan $k = \frac{g \cdot \rho_f \cdot \varepsilon_{mf}}{\mu_f k_c S}$ described in (as cited in Leva, [22]) yield the formula to define the minimum fluidization velocity [22, 23].

$$V_{mf} = \frac{5 \times 10^{-3} (\phi d_p)^2 (\rho_p - \rho_f) g \varepsilon_{mf}^3}{\mu_{mf} (1 - \varepsilon_{mf})} \quad (31)$$

The Leva formula is used in case of Reynolds to be smaller than 10 ($Re_{mf} < 10$). In case of Reynolds to be larger than 10 ($Re_{mf} > 10$), there is an adjustment factor added into this formula.

2.1.9 Determination of V_{mf} according to Kunii-Levenspiel

The formula of Kunii-Levenspiel was simplified from the Ergun formula and it gave out two cases of calculation of the minimum fluidization velocity. In the first case for solid particles of small size with $Re_{mf} < 20$, we have to use Eq. (32).

$$V_{mf} = \frac{(\phi d_p)^2 (\rho_p - \rho_f) g \varepsilon_{mf}^3}{150 \mu_f (1 - \varepsilon_{mf})} \quad (32)$$

We have to use Eq. (33) for the larger particle size with Reynolds number larger than 1000 ($Re_{mf} > 1000$).

$$V_{mf}^2 = \frac{(\phi d_p) (\rho_p - \rho_f) g \cdot \varepsilon_{mf}^3}{1.75 \rho_f} \quad (33)$$

2.1.10 Determination of V_{mf} based on the bed voidage problem

There is a correlation equation of particle mass balance at the minimum fluidization state (fluidization without bubbles), which was created by Kunii and Levenspiel as shown in Eq. (34).

$$g \cdot H_0 (1 - \varepsilon_0) \rho_p \cdot A = (1 - \varepsilon_{mf}) \rho_p g \cdot H_{mf} \quad (34)$$

Thus, we can obtain a correlation as shown in Eq. (35).

$$\frac{H_{mf}}{H_0} = \frac{(1 - \varepsilon_0)}{1 - \varepsilon_{mf}} \quad (35)$$

According to Ginzburg, described in [18], the bed voidage of minimum fluidization and height of particle layer are calculated by Eq. (36) and Eq. (37).

$$\varepsilon_{mf} = \varepsilon_0 \times 10\% \quad (36)$$

$$H_{mf} = H_0 \times 10\% \quad (37)$$

McCabe et al. proposed $\varepsilon_{mf} = 0.4 \div 0.45$ for the spherical particle [24]. The bed voidage of minimum fluidization particle layers was 0.5 ($\varepsilon_{mf} = 0.5$) for larger particle size. The bed voidage is equal to 1.0 ($\varepsilon_t = 1.0$) when the particle layers are attracted to the gas stream (see position C in **Figure 2**).

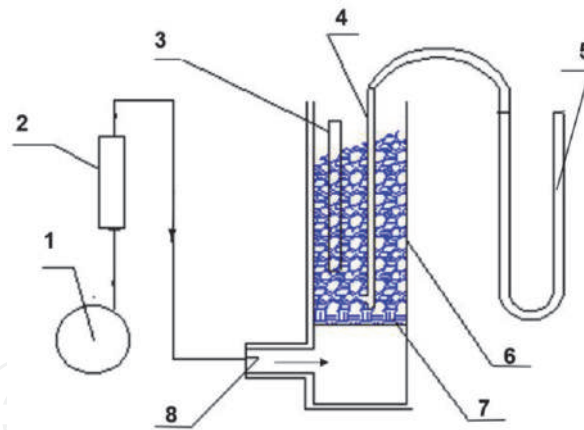


Figure 3. Model for determination of the minimum fluidization velocity. 1. Centrifugal fan; 2. air heater; 3. thermometer for surface particle temperature measurement; 4. pitot tube for measurement of dynamic pressure and total pressure of air; 5. U-manometer; 6. chamber of fluidization; 7. air distributor; 8. drying air inlet.

2.2 Physical model of experiment

Experimental arrangement of determining the minimum fluidization velocity is shown in **Figure 3**.

In order to gradually increase the bed surface velocity of hot air via the particle layers, the air fan (1) is equipped with an inverter to change the rotation of the fan motor.

2.3 Experimental equipment

The instruments in experiments include a moisture analyzer (Axis AGS100, Germany), measurement error $\pm 0.01\%$; a digital electronic scale (Satorius MA45, Germany), measurement error ± 0.001 g; an air velocity meter (Extech SDL350 Taiwan), measurement error ± 0.01 m/s and a digital thermometer (WIKA CTH6300, Germany), measurement accuracy 0.001°C . This instrument has two measuring rate modes including fast at 4/s and slow at 1/s; an inclined manometer (T10, UK), measured range is 0–280 mmwg with error $\pm 0.1\%$ and a pitot pipe (PT6300, 304 Germany), measurement range is 0–400 mmwg with error $\pm 0.1\%$. For measurement on the bulk density and density of refined salt particles, we used instruments such as Graduated pipet, buret, graduated cylinder, all of them made in Germany with error measurement ± 0.01 ml. The HCl acid is used for density measurement of refined salt particles.

No.	Equipment/parts	Technical parameter
1	Drying air fan	Flow: $0.63 \text{ m}^3/\text{s}$; total pressure: 1244 Pa; motor power: 2.2 kW
2	Electrical heater	Overall dimension (L \times W \times H): 600 \times 630 \times 275 mm; heating power: 1.0 kW; number of heater bars: 6
3	Drying chamber	Overall dimension (L \times W \times H): 1750 \times 300 \times 350 mm Fabrication material: SUS304
4	Salt dust settling chamber	Overall dimension (L \times W \times H): 1750 \times 450 \times 350 mm Fabrication material: SUS304

Table 3. The basic parameters of the continuous fluidized bed dryer for experiment by authors.

2.4 The materials of refined salt particles

The material of refined salt particles was supplied by a combined hydraulic separating-washing-grinding machine in the saturated saltwater condition and which was dried by a continuous centrifugal machines. Samples of refined salt were randomly taken at different sizes at Vinh Hao salt company in Binh Thuan Province, Bac Lieu salt company and Sea salt Research Center of Vietnam for analysis (**Table 3**) [14].

3. Results and discussions

The above section presented nine methods to calculate minimum fluidization velocity based on the physical parameters of particles and physical thermal parameters of gas stream. These parameters were obtained from experiments in combination with the correlation calculation or empirical formulas.

In order to have the basis of comparison and accuracy evaluation of each calculating method in comparison with the empirical method, the theoretical calculation was carried out for refined salt particles with diameters of 1.5 mm, 1.2 mm, 0.9 mm, 0.6 mm and 0.3 mm. On the other hand, to achieve empirical result, samples of dried refined salt particles (of which mean-diameter was determined) were taken randomly from a combined hydraulic-separating-washing-crushing machine, presenting various particle sizes of the raw material that was put in the dryer.

3.1 Results of theoretical and empirical calculations for determining V_{mf} of refined salt particles

3.1.1 Some primary conditions for determining the V_{mf} by theoretical calculations

When calculating the pressure drop across a refined salt particle layer, we relied on the empirical results of physical parameters of particles and air (summarized in **Table 4**). Specific notes for each calculating method are as follows:

a. Calculation based on Ergun equations and correlations of pressure

Applying to calculate the minimum fluidization velocity (V_{mf}) for refined salt particles with the fixed bed height (H_0) is 30 mm, the bed voidage (ϵ_0) is 0.5 using Eqs. (35) and (36) to find out the minimum fluidization state including $H_{mf} = 1.1 \times H_0 = 33$ mm; bed voidage $\epsilon_{mf} = 1.1 \times \epsilon_0 = 0.56$. Using the spherical degree value of refined salt particle is 0.71 ($\phi = 0.71$) and other parameters were taken from the **Table 5** which described in Bui (2009). Then we use the Ergun equations to calculate the minimum fluidization velocity. It is recommended that Re_{mf} had no limit [13–15].

b. Calculation based on the correlation between (Re_{mf}), (Ar) and Kozeny-Carman

In these two calculation methods, the parameters in the calculations are taken from the empirical results according to **Table 5**.

c. Determination of the (V_{mf}) value according to Wen and Yu

According to Wen and Yu methods, the bed voidage of the refined salt particle layer at minimum fluidization state (ϵ_{mf}) was unknown, but we had

Determination of the minimum fluidization velocity according to theoretical and empirical methods											
No	d _h (mm)	Minimum fluidization velocity									
		Ergun	Re and Ar	Ko and Ca	Wen and Yu	Gedar	Go	Todes	Leva	Kunii and Levenspiel	Empirical methods
1	1.65	1.327	0.939	3.149	0.5414	0.45	1.1223	1.122	2.362	3.149	0.8
2	1.35	1.094	0.736	2.108	0.4002	0.331	0.9022	0.902	1.581	2.108	0.6
3	1.05	0.826	0.518	1.275	0.2625	0.219	0.6653	0.665	0.956	1.275	0.58
7	0.953	0.731	0.445	1.05	0.2209	0.186	0.586	0.586	0.788	1.05	0.55
4	0.75	0.522	0.298	0.651	0.1416	0.123	0.4188	0.419	0.488	0.651	0.42
5	0.45	0.22	0.115	0.234	0.0524	0.05	0.1863	0.186	0.176	0.234	0.2
6	0.225	0.058	0.029	0.059	0.0132	0.014	0.0537	0.054	0.044	0.059	0.15

The bold values in Table 4 refers to the common average particle size for commercial refined salt in the Vietnamese market.

Table 4.

Theoretical calculation results of minimum fluidization velocity for refined salt particles from equations and empirical correlation formulas of published authors, which compare to the experimental results of the physical model of author.

Technical parameter	Symbol	Unit	Value	Ref.
Refined salt particle diameter	d_p	mm	1.65; 1.35; 1.05; 0.75; 0.45; 0.225	[13, 14] [15]
Average diameter of particle	d_m	mm	0.953	
Static bed voidage	ϵ_0		0.51	
Bed voidage in minimum fluidization velocity	ϵ_{mf}		0.56	
Particle density	ρ_p	kg/m ³	2138	
Bulk density	ρ_b	kg/m ³	982	
Spherical degree of particle	ϕ		0.71	
Gas density (at 160°C)	ρ_f	kg/m ³	0.815	
Dynamic viscosity (at 160°C)	μ_f	kg/m.s	2.45×10^{-5}	
Fixed refined salt particle bed height	H_0	m	30	

Note: The particle diameter $d = 0.953$ is the average diameter of the salt particles.

Table 5.
Physical parameters of refined salt grains and physical air.

the value of spherical degree particle from experiments (see **Table 5**). We put the value of spherical degree into Eq. (5) or Eq. (16) and found out the value of bed voidage (ϵ_{mf}) from which the velocity value of gas passing through the minimum fluidization particle layer (V_{mf}) was calculated.

d. Determination of V_{mf} according to Groshko-Todes

In this method, we also used the results of physical parameters of refined salt particles and air supplied to the dryer from **Table 5** to calculate Ar number. The Re_{mf} is determined by using Eq. 2 and the obtained result was multiplied by the error coefficient $k = 1.2$ and it was considered as the result of calculation of Re_{mf} for non-spherical salt particles (described by Lebedev, [21]). In addition, in Todes method there was another calculation by using Eq. (29) based on the available results of the minimum fluidization velocity ($\epsilon_{mf} = 0.4$). We put this value into Eq. (15) and we found out the spherical degree of salt particles according to correlation given by Wen and Yu. Then we put this value into Eq. (12) to determine Ar number. By replacing Eq. (29) with the value of Ar number, we found out Re_{mf} , from which we could calculate V_{mf} value by using Eq. (10).

e. Determination of V_{mf} by the formula of Beayens-Geldart, Goroshko, Leva, and Kunii-Levenspiel

The minimum fluidization bed velocity (V_{mf}) was determined by using theoretical calculation of formulas of Beayens-Geldart, Goroshko, Leva, and Kunii-Levenspiel with the available physical parameters of refined salt particles and gas given in **Table 5** [18, 19, 22, 25, 26]. **Table 4** shows the calculated results from the formulas of authors published last time.

3.1.2 Primary conditions for determining V_{mf} by experimental method

A model in **Figure 3** and the other of fluidized bed dryer in **Figure 4** was designed by authors to define the minimum fluidization velocity of refined salt

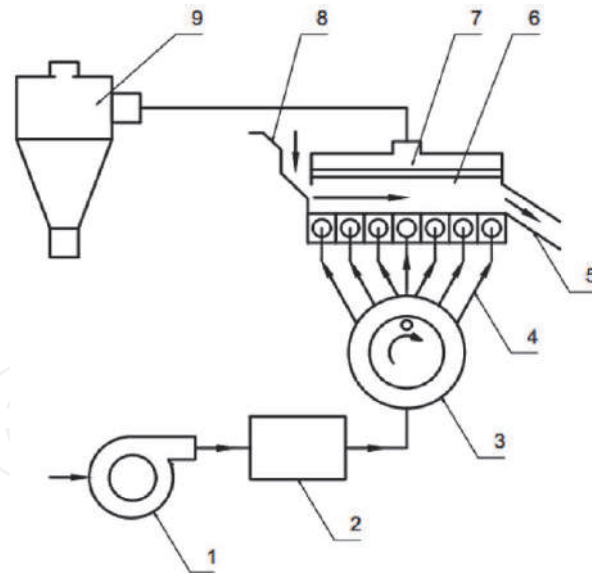


Figure 4.
 The model of continuous fluidized bed dryer used in experiments. 1. Air fan; 2. heating chamber; 3. air supplier; 4. air duct; 5. product outlet; 6. drying chamber; 7. dust separation chamber; 8. inlet feeder; 9. cyclone dust collector.

particles in experiment. The dryer model was designed with its capacity of 48 kg/hour, the height of salt particle layer at the static bed was 30 mm ($H_0 \geq 30$ mm). In the experiments, the authors determined the minimum fluidization velocity (V_{mf}) for refined salt particles with diameter 1.65, 1.35, 1.05, 0.9, 0.65, 0.4 and 0.3 mm. The experimental results of determination of the minimum fluidization velocity of the particle layers with the different particle sizes are shown in **Table 4**. Besides, these experimental minimum fluidization velocity values were also compared with results of theoretical models that were published by authors presented in the methodology part above (**Figure 5**).

3.2 Discussions

- The obtained values of minimum fluidization velocity (V_{mf}) calculated by the Ergun equation and the correlation between Re_{mf} number and Ar number for

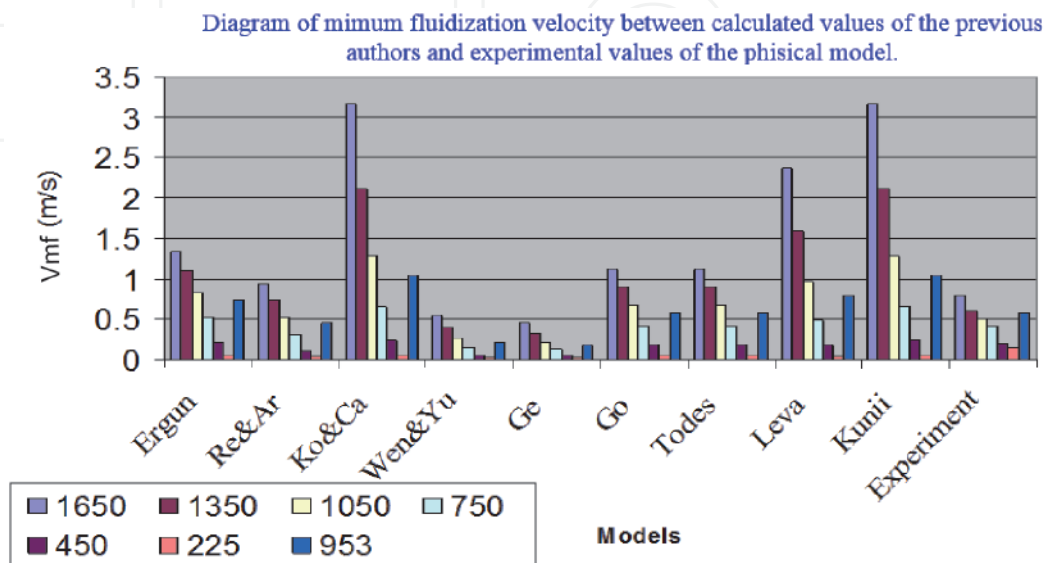


Figure 5.
 Comparison of the minimum fluidization air velocity between calculated values of published authors and experimental values of the model [14].

all particle sizes agreed well with the experimental values. The value of Re_{mf} number varies from 0.3 to 51.7. Particles with sizes $d_p = 0.225; 0.45$ and 0.75 had the tendency for laminar flow.

- The obtained values of minimum fluidization velocity (v_{mf}) determined by the Kozeny-Carman and Kunii equations for particles with diameter greater than 1 mm ($d_p > 1\text{ mm}$) were much larger than experimental values ($V_{tmf} \gg V_{emf}$). While, with particles having diameter smaller than 1 mm ($d_p < 1\text{ mm}$), the result of calculation was nearly equal to the experimental values. Notably, the void fraction value of the minimum fluidization state from 0.4 to 0.5 ($\epsilon_{mf} = 0.4\text{--}0.5$) the calculation result matches the experimental value.
- By using the correlation of Wen and Yu to calculate void fraction at (ϵ_{mf}) knowing the spherical properties of particle, we obtained values that were much smaller than the experimental value. The Re_{mf} number varied from 0.07 to 21.1 .
- When using the correlation between Re_{mf} and Ar , the obtained values of minimum fluidization velocity fit quite well to experimental results. Reynolds values vary from 0.16 to 36.6 .
- The minimum fluidization velocity that was calculated according the correlation between Re_{mf} and Ar number of Beayens and Geldart (Eq. (19)) gave reasonable results.
- The obtained values by using the Goroshko and Todes formula in Eq. (28) were nearly equal to the experimental values.
- The calculated value of V_{mf} according to Beayens and Geldart was the lowest in comparison to other methods.
- The difference between the values of Re_{mf} calculated according to Goroshko and Ergun was lower than $10\text{--}20\%$ for particles that lie in the range of Re_{mf} number from 0.28 to 43.7 ($Re_{mf} = 0.28\text{--}43.7$). The obtained values of velocity value (V_{mf}) for particles with diameter smaller than 0.9 mm ($d_p < 0.9\text{ mm}$) were closer to the experimental value in comparison with particles with diameter larger than 0.9 mm ($d_p > 0.9\text{ mm}$).
- The minimum fluidization velocity that was calculated by Leva formula was only suitable for particles with diameter smaller than 0.75 mm ($d_p < 0.75\text{ mm}$) and value of Re_{mf} number smaller than 10 ($Re_{mf} < 10$). The regime of air flow through the particle layer is laminar flow.
- The calculation method of the minimum fluidization velocity according to the Kunii and Levenspiel equations was suitable for particle with diameter $d_p = (0.225; 0.45; 0.75\text{ mm})$ and the results were appropriate under the conditions $Re_{mf} < 20$, and the calculation result was close to the experimental value.

3.3 Determination of air velocity through the particle layer at the optimum fluidization regime (V_{of})

The optimal fluidization velocity V_{of} was in the region from A to C (**Figure 2**). It meets the conditions:

$$V_{mf} < V_{hf} < V_{cf} \quad (38)$$

The air superficial velocity value from A to C (**Figure 2**) was determined by the two standard equations as follows:

The air velocity through the solid particle layer at the optimum fluidization regime (V_{of}) was calculated according to Fedorov standard (Fe) by Eq. (39) (as cited in Lebedev [21]), with refined salt particles and drying air parameters taken from **Table 5** ($t_f = 160^\circ\text{C}$) [13, 15].

$$Fe = \phi d_p \left(\frac{4g(\rho_p - \rho_f)\rho_f}{3\mu_f^2} \right)^{1/3} \\ = 0.71 \times 0.956 \times 10^{-3} \cdot \left(\frac{4 \times 9.8(2138 - 0.815)0.815}{3 \cdot (2.45 \times 10^{-5})^2} \right)^{1/3} = 32 \quad (39)$$

According to Ginzburg (1973), Re_{hf2} was calculated by Eq. (40) [20, 27].

$$Re_{hf2} = (0.19 \div 0.285) Fe^{1.56} \rightarrow Re_{hf2} = 0.237 \times 32^{1.56} = 53 \quad (40)$$

The homogeneous fluidization velocity (V_{hf1}) was calculated by Eq. (41).

$$V_{hf2} = \frac{\mu_f \cdot Re_{hf}}{\rho_f \cdot d_p} = \frac{2.45 \times 10^{-5} \times 53}{0.815 \times 0.956 \times 10^{-3}} = 1.6 \text{ m/s} \quad (41)$$

Reynolds value at homogeneous fluidization velocity (V_{hf1}) was measured according to Archimedes standard by Eq. (42) [20].

$$Re_{hf1} = (0.22 \div 0.33) \times Ar^{0.52} \quad (42)$$

where Ar was calculated by Eq. (12):

$$Ar = \frac{\rho_f (\rho_p - \rho_f) g (\phi d_p)^3}{\mu_f^2}$$

Substituting parameters of air and refined salt particles into the Eq. (12),

$$Ar = \frac{9.81 \times (0.71(956 \times 10^{-6}))^3 \times 0.815 \times (2138 - 0.815)}{(2.45 \times 10^{-5})^2} = 8818.4$$

The Ar value is 8818.4

Therefore, $Re_{hf1} = 0.275 \times (8818.4)^{0.52} = 66.917 = 31.53$.

The homogeneous fluidization velocity (V_{hf1}) was calculated by Eq. (43).

$$V_{hf1} = \frac{\mu_f \cdot Re_{hf}}{\rho_f \phi d_p} = \frac{2.45 \times 10^{-5} \times 31.53}{0.815 \times 0.956 \times 10^{-3}} = 0.99 \text{ m/s} \quad (43)$$

Re-calculating the homogeneous fluidization velocity (V_{hf1}) by using the experimental equation Eq. (44) [27].

From **Table 4** for the specific case: $V_{mf} = 0.55$ m/s and particle diameter was 0.953 mm.

$$V_{hf1} = (2 \div 3) \times V_{mf} = (2 \div 3) \times 0.56 = (1.12 \div 1.68) \text{ m/s} \quad (44)$$

Both V_{hf1} and V_{hf2} met the conditions of the Eq. (38). Selecting the optimum velocity V_{of} :

$$V_{of} = (V_{hf1} + V_{hf2})/2 = (0.99 + 1.66)/2 = 1.33 \text{ m/s}$$

Re-calculating the standard Reynolds number at reasonable fluidization state (Re_{of}) under the condition of optimum fluidization velocity ($V_{of} = 1.33$ m/s)

$$V_{of} = \frac{\mu_f \cdot Re_{of}}{\rho_f \cdot d_p} \quad (45)$$

or

$$Re_{of} = \frac{\phi d_p \rho_f V_{of}}{\mu_f} = \frac{0.71(0.956 \times 10^{-3})0.815 \times 1.33}{2.45 \times 10^{-5}} = 30$$

The value of optimum Reynolds number (Re_{of}) was 30 ($Re_{of} = 30$).

The void fraction of the particle layer at the reasonable fluidization state was determined by the Zabrodski formula (Eq. 46) (described in Lebedev, [21]).

$$\varepsilon_{hf1} = \left(\frac{18 Re_{ohf} + 0.36 Re_{ohf}^2}{Ar} \right)^{0.21} = \left(\frac{18 \times 30 + 0.36(30)^2}{8818.4} \right)^{0.21} = 0.61 \quad (46)$$

Re_{hf2} could be recalculated according to the correlation between Re_{hf2} and Ar Eq. (47).

$$Re_{hf2} = (0.22 \div 0.33) Ar^{0.52} = 0.275 \times (8818.4)^{0.52} = 31 \quad (47)$$

Substituting value of Re_{hf2} into Eq. (46), we re-calculated the homogeneous fluidization void fraction (ε_{hf}) by Eq. (48).

$$\varepsilon_{hf2} = \left(\frac{18 Re_{hf} + 0.36 Re_{hf}^2}{Ar} \right)^{0.21} = \left(\frac{18 \times 31 + 0.36(31)^2}{8818.4} \right)^{0.21} = 0.62 \quad (48)$$

These two calculation methods generated almost identical results.

3.4 Calculation of the critical air velocity flowing through the fluidization particle layer

In order to have a basis for determining the reasonable dimension of separating chamber of fluidized bed dryer (the chamber was located above the fluidization particle drying tank) and to limit removal of materials from the drying chamber, we defined the theoretical critical velocity (also called the final velocity).

From the calculation result of Re_{mf} of the minimum fluidization state ($Re_{mf} = 10.032$), this parameter of the air stream through the particle layer in the transition flow was in range $1 < Re_{mf} < 500$.

According to the equation of Haider and Levenspiel (described in Wen-ChingYang) [28, 29], the critical velocity was calculated by Eq. (49).

$$V_{cf} = \left[\frac{4(\rho_p - \rho_f)g}{3\rho_f C_D} \phi d_p \right]^{1/2} = \left[\frac{4(2138 - 0.815)9.81}{3 \times 0.815 \times C_D} 0.71 \times 0.953 \right]^{1/2} \quad (49)$$

With resistance coefficient (C_D) (described in Wen-ChingYang) [27, 28] given by

$$C_D = \frac{18}{Re^{3/5}} = \frac{18}{(10.032)^{3/5}} = 4.5 \quad (50)$$

So, the critical velocity at position C (**Figure 2**) in the specific case had the value:

$$\begin{aligned} V_{cf} &= \left[\frac{4(\rho_p - \rho_f)g}{3\rho_f C_D} \phi d_p \right]^{1/2} \\ &= \left[\frac{4(2138 - 0.815) \times 9.81}{3 \times 0.815 \times 4.5} (0.71 \times 956 \times 10^{-6}) \right]^{1/2} = 2.3m/s \end{aligned} \quad (51)$$

In fact, during the drying process, to ensure the drying productivity and quality, the dryer operator must observe the fluidization particle layer and adjust the inlet doors of drying air capacity at appropriate the air velocity value in the range from A to C (**Figure 2**) and the correlation of velocity types $V_{mf} < V_{hf} < V_{cf}$.

We re-calculated the void fraction of particle layer with average particle diameter $d_p = \phi d_m = 0.953$ mm at the theoretical critical velocity in fluidization particle layer condition.

$$Re - \text{calculating } Re_{cf} : Re_{cf} = \frac{\phi d_p \cdot \rho_f \cdot V_{cf}}{\mu_f} \quad (52)$$

Substituting the above value into Eq. (52), we get:

$$Re_{cf} = \frac{0.71 \times (956 \times 10^{-6}) \times 0.815 \times 2.3}{2.4 \times 10^{-5}} = 0.53.$$

Using Eq. (46) to re-calculate the void fraction of particle layer at the complete fluidization state:

$$\varepsilon_{tf} = \left(\frac{18 Re_{cf} + 0.36 Re_{cf}^2}{Ar} \right)^{0.21} = \left(\frac{18 \times 53 + 0.36 \times (53)^2}{8818.4} \right)^{0.21} = 0.73$$

When the void fraction of particle layer was 1 ($\varepsilon = 1$), the fluidization particle layer turned to the transport regime in the air stream (called pneumatic transportation).

4. Conclusions

Most of the used correlations in the calculations and the formulas given by the authors, as mentioned above, were derived from the experiments with temperature close to the ambient temperature. So, when we use them in calculations in specific cases, they should consider the accuracy. The extrapolation should be used in the cases of the states at the temperature higher than the ambient temperature.

The mentioned theoretical calculations show the necessity for the determining of the minimum fluidization velocity of the solid particle layer with high accuracy. The sphericity of particle and void fraction of the particle layer were often not known, therefore it is required to get their values from the range of experimental variables. Empirically, the void fraction of the particles in the minimum fluidization layer at the ambient temperature is not the same as that in the increasing gas temperature.

The best method to determine the minimum fluidization velocity is to conduct the experiments. Firstly, we directly measured the pressure drop across the particle layer when the air velocity gradually decreased. Secondly, we built the graphs and read the results of the minimum fluidization velocity value.

However, if we were forced to find out the fluidization velocity without carrying out experiments to measure the pressure drop across the particle layer, the best way would be to determine the void fraction at the minimum fluidization velocity. Then we calculated the spherical property of the particle using the Ergun equations or correlation between Ar and Re_{mf} in Eqs. (10)–(12) to count out the minimum air velocity through the particle fluidization layer. This velocity value also had accuracy close to the experimental one.

The average particle diameter considered spherical degree of the particles of different sizes was $953 \mu\text{m}$ ($d_m = 953 \mu\text{m}$). This diameter represented the size of the particles in dry grinding technology with the hammer crusher. It is also in the common size distribution range of the combined washing-grinding hydraulic-separation technology in Vietnam's market. Besides, the particle diameter of $953 \mu\text{m}$ ($d_p = 953 \mu\text{m}$) is also used in calculating the value of all types of velocity, characterized for the medium particle size of the refined salt production technology in Vietnam.

We calculated the values of three characteristic velocity types of fluidized bed drying for particles with average size $d_m = d_p = 953 \mu\text{m}$, including the minimum fluidization velocity $V_{mf} = 0.55 \text{ m/s}$ with void fraction $\epsilon_{mf} = 0.56$; reasonable fluidization velocity $V_{hf} = 1.33 \text{ m/s}$ corresponding to the void fraction of particle layer $\epsilon_{hf} = 0.615$; and the critical velocity of the air flow through the particle bulk $V_{cf} = 2.3 \text{ m/s}$ with the void fraction value of fluidization particle layer $\epsilon_{cf} = 0.73$.

In fact, during the drying process, to ensure the drying productivity and quality, the dryer operator must observe the fluidization particle layer and adjust the inlet doors of drying air capacity at appropriate air velocity value in the range from A to C (**Figure 2**) to make sure the correlation of velocity types $V_{mf} < V_{hf} < V_{cf}$.

Nomenclature

A	cross sectional area of the bed
m^2	area for gas distribution
H	height of the bed, m
Ar	Archimedes number, dimensionless
H_0	initial bed height, m

ε_0	void fraction at static particle layer
H_{mf}	minimum fluidization bed height, m
ε_{mf}	void fraction at minimum fluidization particle layer
ΔP	pressure drop across the bed, N/m ²
ε_{hf}	void fraction at homogeneous fluidization particle layer
Re	Reynolds number
ε_{tf}	terminal void fraction
Re_{mf}	Reynolds number at the minimum fluidization velocity
Re_{hf}	Reynolds number at the homogeneous fluidization velocity
d_p	spherical particle diameter, m
ϕd_m	equivalent spherical mean diameters, m
Re_{cf}	Reynolds number at the fluidization terminal velocity
ϕ	sphericity degree, dimensionless
Re_{of}	Reynolds number at the optimum fluidization velocity
Fe	Fedorov standard, dimensionless
V	bed surface velocity or superficial velocity, m/s
g	acceleration due to gravity, m/s ²
V_{mf}	minimum fluidization velocity, m/s
ρ_p	solid particle density, kg/m ³
V_{tmf}	theoretical minimum fluidization velocity, m/s
ρ_b	particle bulk density, kg/m ³
V_{emf}	experimental minimum fluidization velocity, m/s
ρ_f	air density, kg/m ³
V_{hf}	homogeneous fluidization velocity, m/s
Kcc	Kozeny-Carman coefficient
V_{ohf}	optimum homogeneous fluidization velocity, m/s
m_p	mass of particles, kg
V_{cf}	terminal velocity or critical velocity, m/s
m_b	mass of particles bulk, kg
μ	air dynamic viscosity, kg/ms
S_s	specific surface area, cm ⁻¹ , cm ² /g
U	cubic volume of particle layer, m ³
W	weight of particle, mass, N

Author details

Bui Trung Thanh^{1*} and Le Anh Duc^{2*}

1 Industrial University of Ho Chi Minh City, Vietnam

2 Nong Lam University, Ho Chi Minh City, Vietnam

*Address all correspondence to:

buitrungthanh@iuh.edu.vn and leanhduc@hcmuaf.edu.vn

IntechOpen

© 2020 The Author(s). Licensee IntechOpen. This chapter is distributed under the terms of the Creative Commons Attribution License (<http://creativecommons.org/licenses/by/3.0/>), which permits unrestricted use, distribution, and reproduction in any medium, provided the original work is properly cited. 

References

- [1] Tavoulaareas S. Fluidized-bed combustion technology. Annual Reviews. 1991;**16**:25-27
- [2] Lewis WK, Gilliland ER, Bauer WC. Characteristics of fluidized particles. Industrial and Engineering Chemistry. 1949;**41**:1104-1117. DOI: 10.1021/ie50497a059
- [3] Zahed AH, Zhu JX, Grace JR. Modelling and simulation of batch and continuous fluidized bed dryers. Drying Technology. 1995;**13**:1-28. DOI: 10.1080/07373939508916940
- [4] Han JW, Keum DH, Kim W, Duc LA, Cho SH, Kim H. Circulating concurrentflow drying simulation of rapeseed. Journal of Biosystems Engineering. 2010;**35**(6):401-407. DOI: 10.5307/JBE.2010.35.6.401
- [5] Hong SJ, Duc LA, Han JW, Kim H, Kim YH, Keum DH. Physical properties of rapeseed (II). Journal of Biosystems Engineering. 2008;**33**(3):173-178. DOI: 10.5307/JBE.2008.33.3.173
- [6] Duc LA, Han JW. The effects of drying conditions on the germination properties of rapeseed. Journal of Biosystems Engineering. 2009;**34**(1): 30-36. DOI: 10.5307/JBE.2009.34.1.030
- [7] Abrahamsen AR, Gedart D. Behaviour of gas-fluidized beds of fine powders part I. Homogeneous expansion. Powder Technology. 1980; **26**:47-55. DOI: 10.1016/0032-5910(80)85006-6
- [8] Geldart D. The effect of particle size and size distribution on the behaviour of gas-fluidized beds. Powder Technology. 1972;**6**:201-215
- [9] Geldart D. Types of gas fluidization. Powder Technology. 1973;**7**:285-292. DOI: 10.1016/0032-5910(73)80037-3
- [10] Howard JR. Fluidized Bed Technology: Principles and Application. Publisher Taylor and Francis Group; 1989. p. 214
- [11] Rhodes M. Fluidization of particles by fluids. In: Educational Resources for Particles Technology. Melbourne, Australia: Monash University; 2001. pp. 1-39
- [12] Ergun S. Fluid flow through packed columns. Chemical Engineering Progress. 1952;**48**:9-94
- [13] Bui TT. Determination on geometrical parameters of refined salt particle applying of fluidized particle lay drying. Journal of Heat Science and Technology. 2009;**86**:10-13
- [14] Bui TT. Determination on hydrodynamic parameters in fine salt drying in a model of fluidized bed dryer. Journal of Heat Science and Technology. 2009;**90**:13-17
- [15] Bui TT. Researching and determining on basic physical parameters of refined salt particles to apply in the calculation and designing of continuous fluidized bed. Journal of Vietnam Mechanical Engineering. 2009; **146**:8-31 and 48
- [16] Yates JG. Fundamentals of Fluidized-Bed Chemical Processes. 1st ed. Oxford: Butterworth-Heinemann; 1983. p. 236
- [17] Wen CY, Yu YH. A generalized method for predicting the minimum fluidized velocity. AIChE Journal. 1966; **12**:610-612
- [18] Baeyens J, Geldart D. Predictive calculations of flow parameters in gas fluidized bed and fluidization behavior of various powders. In: Proceedings of

the International Symposium on
Fluidization and its Applications; 1973

[19] Goroshko VD, Rozenbaum RB,
Todes OM. Approximate laws of
fluidized bed hydraulics and restrained
fall. *Izvestiya Vysshikh Uchebnykh
Zavedenii, Neft i Gaz*. 1958;1:125-131

[20] Tran VP. Calculation and Designing
on the Drying System. Hanoi: Education
Publishing House; 2002

[21] Lebedev PD. Calculation and Design
of Drying Equipmet. Moscow,
Leningrad: Gosenergoizdat; 1963. p. 320
(in Russian)

[22] Leva M. Fluidization. New York:
McGraw-Hill; 1959. p. 281

[23] Carman PC. Fluid flow through
granular beds. *Transactions, Institution
of Chemical Engineers*. 1937;15:150-166

[24] McCabe WE, Smith JC, Harriott P.
Unit Operations of Chemical
Engineering. 6th ed. New York:
McGraw Hill; 2001. p. 1132

[25] Kunii D, Levenspiel O. Various
kinds of contacting of a batch of solids
by fluid. In: *Fluidized Engineering*.
Huntington, NY: Robert E. Krieger
Publishing Co.; 1977. pp. 24-56

[26] Kunii D, Levenspiel O.
Fluidization engineering. 2nd ed.
Boston: Butterworth-Heinemann;
1991. p. 49

[27] Ginzburg AS. Theoretical and
Technical Basis of Drying Food
Products. Moscow: Pishchevaya
Promyshlennost; 1973. p. 528
(in Russian)

[28] Yang WC. Particle characterization
and dynamics. In: Yang WC, editor.
*Handbook of Fluidization and Fluid-
Particle System*. New York: Marcel
Dekker; 2003. pp. 1-29

[29] Yang WC. Flow through fixed beds.
In: Yang W-C, editor. *Handbook of
Fluidization and Fluid-Particle System*.
New York: Marcel Dekker; 2003.
pp. 29-53

We are IntechOpen, the world's leading publisher of Open Access books Built by scientists, for scientists

6,300

Open access books available

171,000

International authors and editors

190M

Downloads

Our authors are among the

154

Countries delivered to

TOP 1%

most cited scientists

12.2%

Contributors from top 500 universities



WEB OF SCIENCE™

Selection of our books indexed in the Book Citation Index
in Web of Science™ Core Collection (BKCI)

Interested in publishing with us?
Contact book.department@intechopen.com

Numbers displayed above are based on latest data collected.
For more information visit www.intechopen.com



The Study of Fabric Drying Using Direct-Contact Ultrasonic Vibration

Chang Peng and Saeed Moghaddam

Abstract

Our existing cloth drying technology is an energy-intensive process, which generally involves blowing hot air across tumbling wet fabrics to facilitate evaporation and moisture removal. To address the relatively low energy efficiency of existing cloth drying techniques, in this chapter, a totally new cloth drying technology is introduced, which uses high frequency ultrasonic vibrations generated by piezoelectric transducer instead of thermal heating to extract moisture in cloth as a cold mist, dramatically reducing drying time and energy consumption. The physical mechanism of ultrasonic fabric drying process in direct-contact mode is first studied. A novel ultrasonic transducer driving method, in which the power supply to the transducer is regulated by a binary modulating signal, is then developed for use in direct-contact ultrasonic drying of fabrics. A demonstration unit is finally fabricated to show the efficacy of the process and its energy saving compared to thermal drying process.

Keywords: fabric drying, energy efficiency, ultrasonic vibration, ultrasonic transducer, physical mechanism

1. Introduction

Clothes dryers offer a rapid means to dry laundry in households but consume substantial residential electricity. Clothes dryers are the second largest source of residential energy use in a household following water heater [1]. Every year the operation of clothes dryers in the United States consumes as much electricity as does the entire state of Massachusetts (60 billion kWh per year) [2]. The demand of clothes dryers in U.S. has increased by nearly 6% over the last decade. Until 2009, 80% of U.S. households had a clothes dryer and 80% of them are electric clothes dryers, the remaining being gas dryers [3]. Although a set of technologies such as air-vented dryers and heat pump dryers have been introduced to the market, the energy efficiency of clothes dryers has not been improved significantly over the last 20 years.

In the current clothes dryer architecture, the clothes dry by passing hot air over the wet fabric. The state of the art for clothes drying technology involves mechanical (centrifugal) water extraction in the washing machine followed by thermal drying in a dryer. The moisture initially extracted by the washing machine reduces the remaining moisture in the clothes to ~50% of the dry weight [4]. The clothes are then placed in a dryer drum, where the remaining moisture is removed by circulating heated air through them. Thermal water removal from clothes in all existing

Dryer type	Average drying time (min)	Energy factor (lb/kWh)
Electric standard (≥ 4.4 ft ³ capacity) [3]	40	3.73
Electric compact (120 V, ≤ 4.4 ft ³ capacity) [3]	40	3.61
Electric compact (240 V, ≤ 4.4 ft ³ capacity) [3]	35	3.27
Gas standard [3]	35	3.30
Heat pump [2]	82	7.6

Table 1. Average clothes drying time and energy factor (EF) values for different types of commercialized clothes dryers.

dryer technologies [3, 5–10] (including heat, heat pump, vacuum, or microwave drying) requires a heat source to provide a latent heat of evaporation of about 2.5 MJ/kg water. The heat source for a dryer can be electric resistance, natural gas and/or an electric heat pump.

The metrics to measure the drying efficiency of a clothes dryer is called energy factor (EF), which commonly has three different types of definitions, depending on how the drying effect is qualified: (1) the mass of moisture removed per energy consumption; (2) the mass of cloth dried per energy consumption; or (3) the latent heat of moisture removed per energy consumption. In the United States, the Department of Energy standard of EF measures the mass of cloth (saturated to certain water content) that can be dried per unit of electricity consumed (lb/kWh) [3]. For gas dryers, it measures the pounds of clothes being dried per equivalent kilowatt-hour of natural gas consumed. Here, we focus on EF (lb/kWh) which is commonly used in the United States. **Table 1** summarizes the EF values for the typical types of existing clothes dryers.

Recently, for the first time, we have introduced a totally new cloth drying technology and are collaborating with Oak Ridge National Laboratory (ORNL) researchers to develop the world's first direct-contact ultrasonic cloth dryer that could potentially change the concept of residential heat-drying technology [11–15]. This novel approach uses high-frequency mechanical vibrations generated by piezoelectric ceramics instead of heat to extract moisture as a cold mist, dramatically reducing drying time and energy use. On the basis of inverse piezoelectric effect, when an electric field is applied in the polarization direction of piezoelectric ceramics, the ceramics will produce mechanical deformation in a certain direction. When a high frequency electric field is applied, the piezoelectric transducer generates acoustic vibration. If the oscillation frequency is larger than 20 kHz, it generates ultrasonic waves that propagate through its surrounding media [12, 16]. Coming to the studies reported on ultrasonic cloth drying per se, to our knowledge, Khmelev et al. [17, 18] is the only paper on this topic. However, a non-contact technique was used in their study, making our study unique and the first of its kind.

This study will address the feasibility of adopting the ultrasonic technique for cloth drying with the objective of achieving lower power consumption and process duration compared to the existing energy-intensive, thermal-based clothes dryers.

2. Experimental setup and method

A schematic of the experimental setup for studying both the water droplet atomization and the fabric drying process is shown in **Figure 1**. The setup mainly consists of six components: an ultrasonic transducer, a function generator, a power

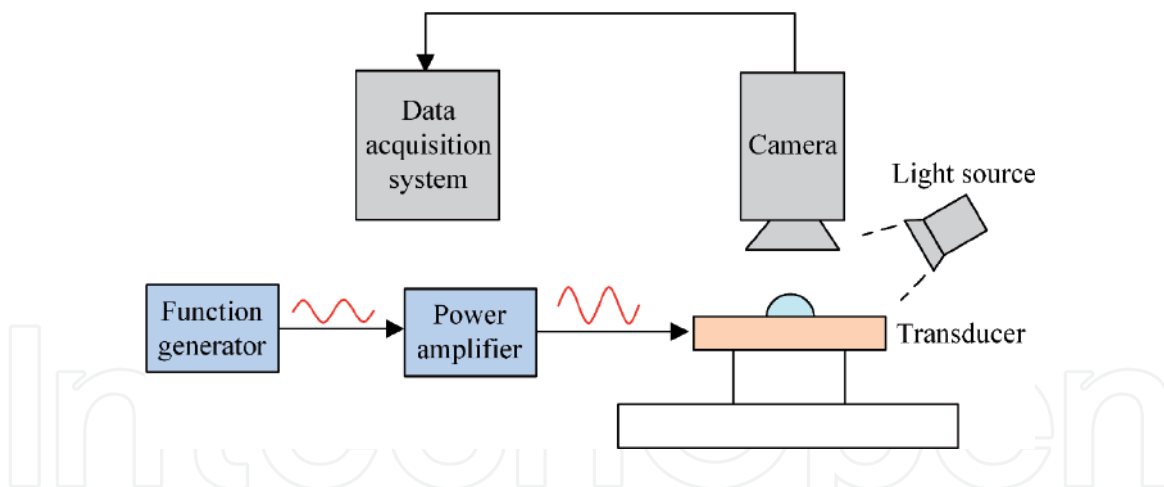


Figure 1.
 Schematic representation of the experimental setup for droplet atomization and fabric drying studies [11].

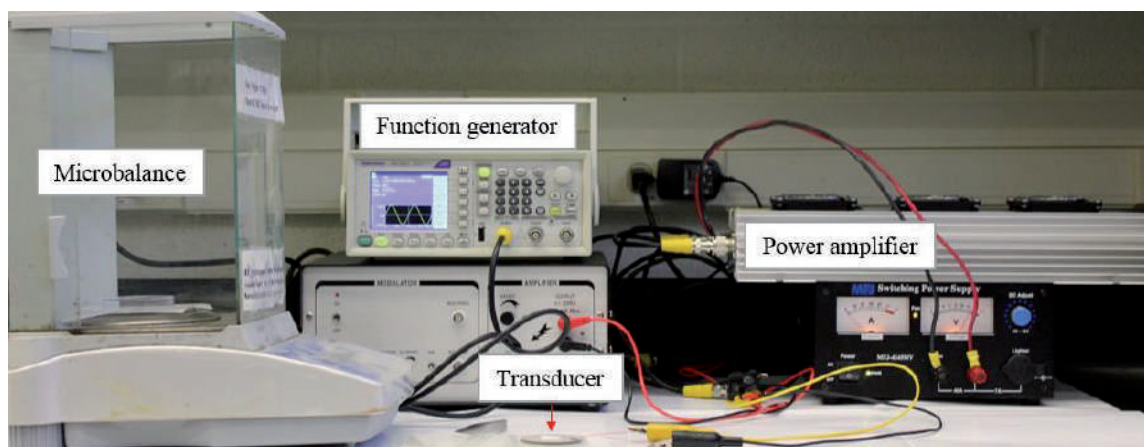


Figure 2.
 Experimental setup for fabric drying study [11].

Transducer	Working diameter (mm)	Resonant frequency (kHz)	Type
A	20	1600	Piezo crystal
B	50	1060	Piezo crystal
C	4.2	135	Metal mesh

Table 2.
 Parameters of transducers tested in this study [11].

amplifier, a high-speed camera, an infrared (IR) camera and a microbalance with a resolution of 0.1 mg for measuring the fabric weights. An image of the experimental setup is provided in **Figure 2**.

The detailed characteristics of the transducers tested in this study are summarized in **Table 2**. Transducer A and B are traditional piezoelectric transducers, the working surfaces of which consist of a piezoelectric ceramic, as shown in **Figure 3a–b**. Transducer C is a metal mesh-based transducer, which consists of a thin metal mesh sandwiched between two piezoelectric rings (**Figure 3c**) that vibrate the mesh. If a water droplet is in direct contact with the mesh surface, the metal mesh-based transducers allow water to pass through the mesh.

For the water droplet atomization study, a water droplet of a specified volume was deployed at the center of the transducer by using a micro-pipette. The atomization process was monitored using the high-speed camera at a frame rate of 3600

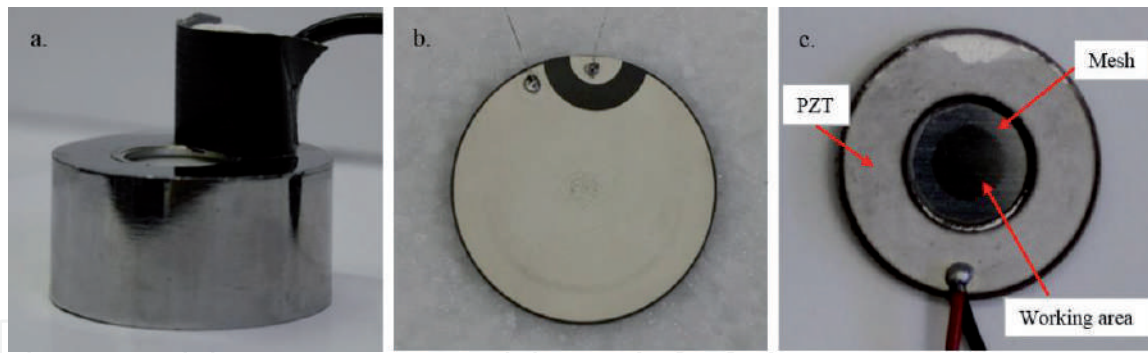


Figure 3. Images of the transducers used in this study: (a) transducer A, (b) transducer B, and (c) transducer C [11].

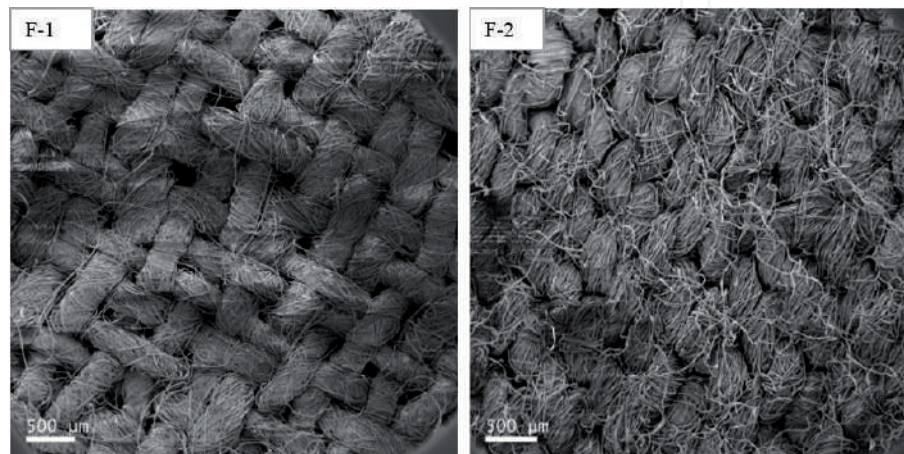


Figure 4. Scanning electron microscope images of the two DOE fabrics [11].

frames per second. The camera line of view was normal to the vibrating surface, thus providing top-view images of the atomizing droplets (**Figure 1**) [11]. During the water droplet atomization process, the IR camera was also used to monitor the droplet and transducer temperature changes. It was mounted in the same way as the high-speed camera. Trials were performed with the following values of the initial droplet volume: 10, 50, and 100 μL .

In the studies, two kinds of US Department of Energy (DOE) standard fabrics (hereinafter called F-1 and F-2) were tested. The SEM images of the fabrics are shown in **Figure 4**. As can be seen from **Figure 4**, F-1 has larger major pore sizes than F-2. Details on the contents, thicknesses and densities for these two fabrics can be found in Ref. [11].

In the studies, the microbalance, AL104, with an error of 0.1 mg was used to measure the weight of the saturated and unsaturated fabric samples to determine the volume of water remaining in the fabric. Prior to the drying test, the dry fabric was placed on the transducer and the weight of this system was measured on the microbalance. After this measurement, the fabric was wet with a known volume of water. The transducer was then actuated to begin the drying process. After 5 s elapsed, the transducer was turned off and the weight of the transducer-fabric system was measured. Immediately after this measurement, the fabric was completely dried by heating it to 80°C. The fabric was then rewet and the weight of the transducer-fabric system was measured after actuating the transducer for 10 s. The fabric was then completely dried. In this manner, the weight of an initially saturated transducer-fabric system was measured after actuating the transducer in increments of 5–10 s, with the fabric dried after each measurement. For each time

interval, the tests were repeated for at least three times. The measurements were recorded until the weight of the transducer-fabric system was less than 5% of the initially saturated system. This method of determining the drying rate of fabrics was repeated for the two fabrics on the three transducers.

3. Ultrasonic atomization of water droplet

Figure 5 illustrates the high-speed images recorded during the atomization of a 10 μL water droplet on transducer A. A qualitative analysis of these images can provide clues to the kinetics of the atomization process. In the initial stage after the transducer was turned on, the oscillations of the transducer surface were transmitted to the surface of the droplet resulting in the formation of capillary waves (**Figure 5b**). As time progressed, the capillary waves grew to form surface ligaments (**Figure 5c**), followed by the atomization of droplet (**Figure 5d–j**), which the droplet broke up via ejection of secondary droplets. The atomization of the droplet exhibited a very chaotic dynamic. In addition to the production of fine mist from the droplet surface, the droplet was observed to spread and deform during the process. [11].

The observed kinematics of droplet atomization can be explained by analyzing the relative magnitudes of the oscillation force (F_o) and surface tension force (F_s) influencing the process [11]. Assuming that the droplet forms a half-sphere on the transducer surface (**Figure 6**), the scale of F_o applied on the water droplet (droplet mass, m_{drop} , and density, ρ) can be presented as,

$$F_o \sim m_{drop} A \omega^2 \sim \frac{1}{12} \pi d^3 \rho A \omega^2 \quad (1)$$

where A and ω are the vibration amplitude and angular frequency ($\omega = 2\pi f$), respectively. On the other hand, the scale of the surface tension force (F_s) experienced by the droplet surface can be presented as [19],

$$F_s = \sigma \pi d \cos\theta \quad (2)$$

where σ is the liquid surface tension which is temperature (T) dependent; d is the droplet diameter which varies with time (t); and θ represents the contact angle formed at the liquid–solid interface.

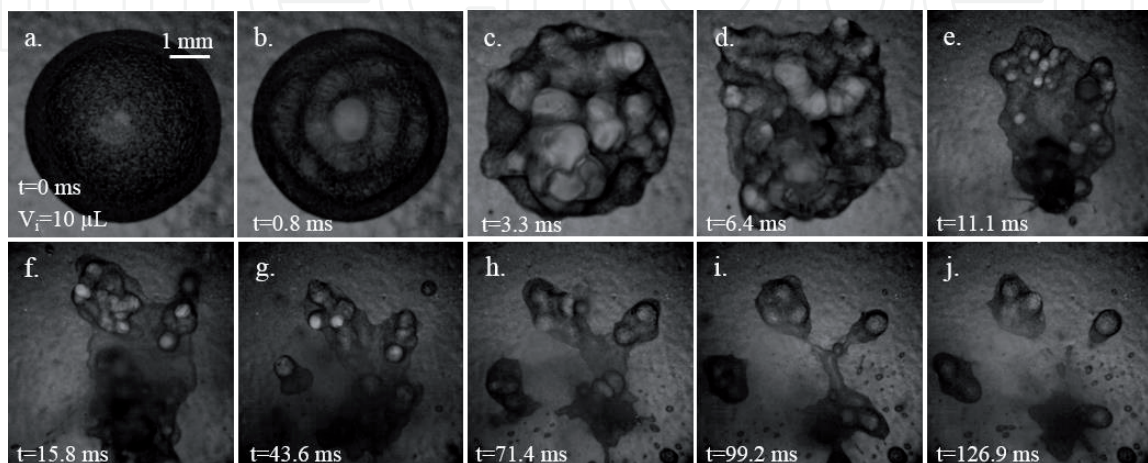


Figure 5. Different regimes of droplet atomization process on transducer A: (a) unperturbed droplet, (b) capillary wave regime, (c) ligament regime, and (d)–(j) catastrophic drop breakup and atomization [11].

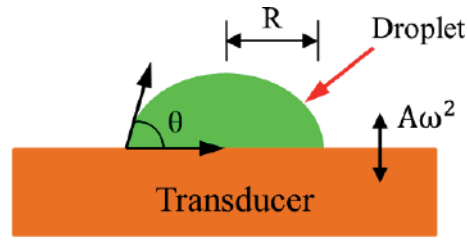


Figure 6. Schematic of a water droplet on a vibrated transducer surface.

The relative magnitude of F_o and F_s can be expressed as,

$$R \sim \frac{F_o}{F_s} \sim \frac{d^2 \rho A \omega^2}{12 \sigma \cos \theta} \quad (3)$$

For a 10 μL water droplet on transducer A (**Figure 5a**), $F_o > F_s$ (i.e. $R > 1$) when the transducer was turned on. This caused the liquid–vapor interface to rupture (leading to atomization), reducing the droplet radius (r) and R . The atomization continued with time until $F_s > F_o$ (at a critical volume), at which point, the atomization process ceased.

During the ultrasonic droplet atomization process, the droplet temperature was also changed due to the viscous dissipation of continuous vibration. And as illustrated in Eq. 3, the surface tension of the droplet (σ) is temperature (T) dependent. Higher the droplet temperature, lower the surface tension will be. The lower surface tension will result in the lower surface tension force (F_s) (Eq. 3). In the following section, the temperature changes on the two types of transducers, piezoelectric crystal transducer and metal mesh transducer, were studied during the droplet atomization process.

Three different volumes of water, 10, 50, and 100 μL , were tested on transducers A, B and C. The thermal responses of these droplets were recorded using the IR camera and the maximum liquid temperature was extracted from this data. **Figure 7** presents the temporal variations in the maximum temperatures of these droplets on transducers. The x -axis represents a non-dimensional time (t^*) defined as

$$t^* = \frac{t}{t_0} \quad (4)$$

where t_0 represents the total duration of time that was recorded using the IR camera (**Tables 3 and 4**).

As can be seen from **Figure 7a**, the temperature for 10 μL droplet varied little immediately after the transducer A was actuated. The temperature went up to

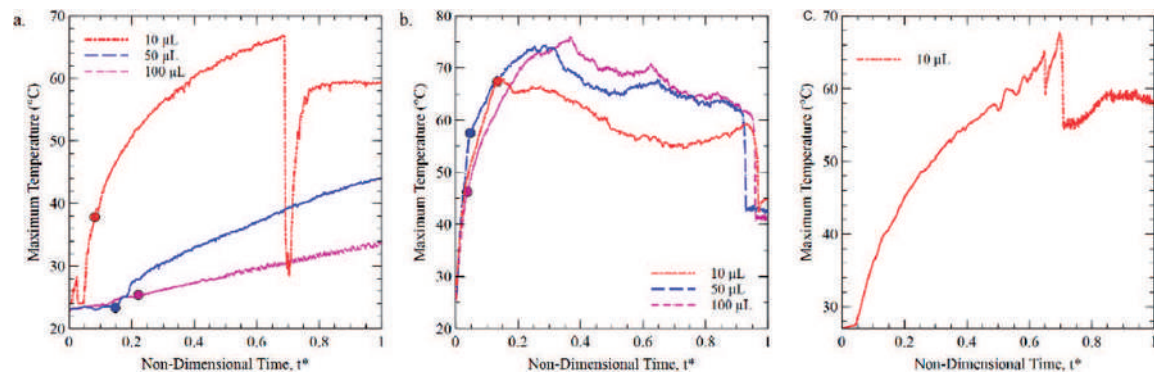


Figure 7. The maximum temperature of liquid on the surface of (a) transducer A, (b) transducer B and (c) transducer C, extracted from the IR images recorded during liquid atomization [11].

Initial volume (μL)	Process time, t_o (s)		
	Transducer A	Transducer B	Transducer C
10	3.29	157.33	31.83
50	3.23	248.67	—
100	2.43	265.00	—

Table 3.
 Summary of the total process time for different droplet volumes on transducers A, B and C [11].

Droplet volume (μL)	Non-dimensional time (t^*)	Threshold temperature ($^{\circ}\text{C}$)
10	0.13	67.4
50	0.05	57.5
100	0.04	46.3

Table 4.
 Threshold temperature and non-dimensional time at which atomization was induced on transducer B [11].

the peak value and then went down sharply. After that process, the temperature increased again and then kept stable. However, for 50 and 100 μL droplet, the temperature just showed the increase in the whole process in **Figure 7a**. And the maximum temperature was much smaller than that of the 10 μL droplet on transducer A. As discussed before, $F_o > F_s$, the droplets could be burst out on transducer A immediately after the transducer was actuated. Meanwhile, the temperature on transducer A kept stable in this tiny time interval as shown in **Figure 7a**. After that the temperature increased due to the viscous dissipation.

For the transducer B in **Figure 7b**, $F_o < F_s$ when the transducer was turned on, the water droplet just vibrated continuously on the transducer B. And because of viscous energy dissipation, the temperature of the droplet went up quickly during the droplet vibrations as shown in **Figure 7b**. When the temperature on transducer B reached a peak value, the droplet on transducer B began to break up. As discussed before, this was because the surface tension of water (σ) decreased with the increase of temperature (T) and $F_s < F_o$. Meanwhile, when the secondary droplets were burst out, the temperature on transducer B decreased continuously.

For the droplet 10 μL on the transducer C, $F_o > F_s$ when the transducer was turned on, large amounts of droplets were jetted out. At this small time interval the temperature on transducer C kept stable, which was similar to the thermal response of the 10 μL droplet on transducer A.

4. Ultrasonic drying behavior of fabric under continuous driving

The baseline dewatering time of fabrics was determined by thermally drying two different saturated fabrics (F-1 and F-2) with the size $4 \times 4 \text{ mm}^2$ at 80°C (**Figure 8**). The saturation volumes for the $4 \times 4 \text{ mm}^2$ fabrics, F-1 and F-2, were ~ 6.45 and $\sim 8.55 \mu\text{L}$ respectively. It was observed that the water content in a given fabric (via thermal evaporation) varied linearly with time (**Figure 8**), since it was directly related to the amount of water stored in the fabric.

Figure 9 demonstrates the drying characteristics of saturated fabrics F-1 and F-2 on transducers A, B, and C. The fabric size was selected such that the sample area did not exceed the working area of the transducers. It was seen that water

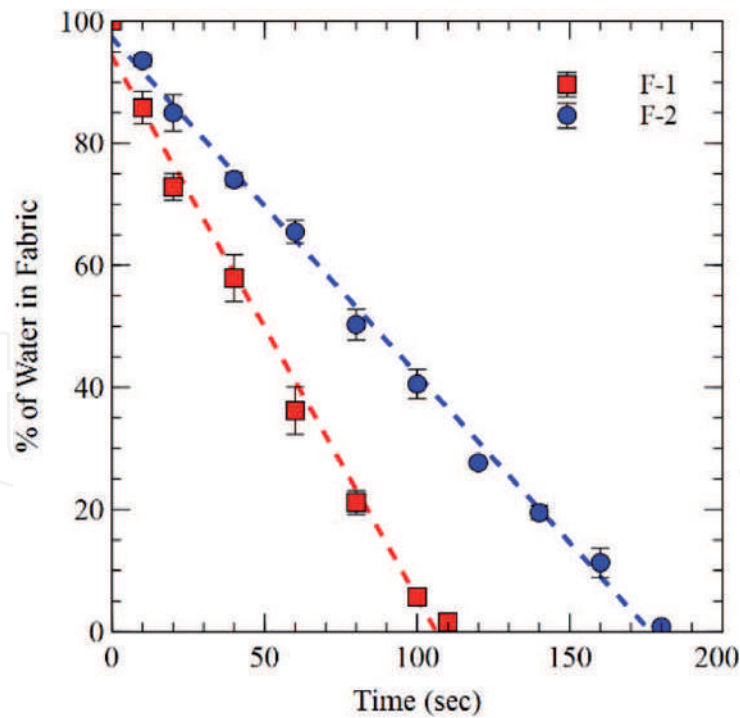


Figure 8.
Thermal drying behavior of two different fabrics [11].

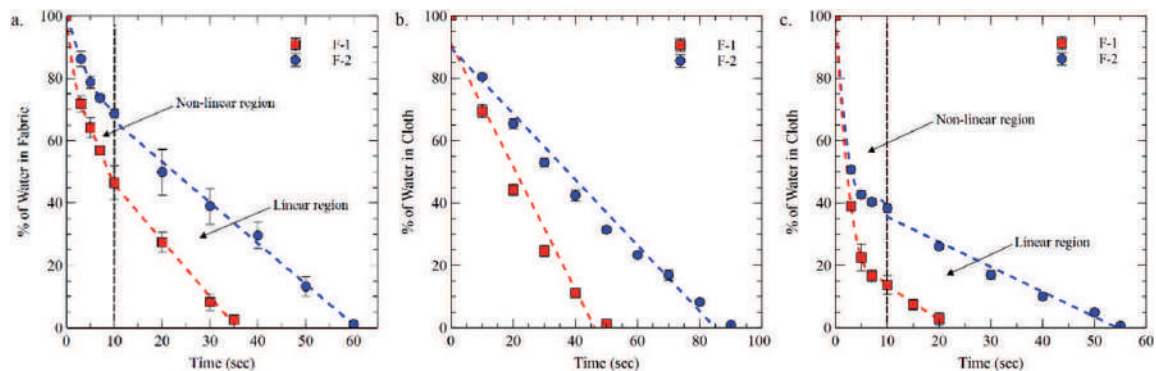


Figure 9.
Drying behavior of different types of fabric on (a) transducer A, (b) transducer B, and (c) transducer C [11].

shedding via ultrasonic excitation dewatered fabrics quicker than thermal drying (**Figure 8**), with up to an 82% reduction in drying time for fabric F-1 on transducer C. The data in **Figure 9** show that the drying curve for each fabric on transducers A and C consist of two distinct regions (indicated by the arrows in **Figure 9**):

- An initial region where the water content in the fabric decreases non-linearly with time;
- A second region where the water content in the fabric decreases linearly with time.

These two regions of the drying curve arise due to the impact of the two major forces involved in the water shedding process—the oscillation force (F_o) and the surface tension force (F_s). There are two kinds of pores in the fabrics: the large pores between the fabric threads and the small pores within the fabric threads (**Figure 4**). Due to the pore size distribution in the fabric, the surface tension force (F_s) in the fabric spans a range of values—large pores in the fabric generate low F_s while small

pores generate large F_s . At $t^* = 0$, the oscillation force generated by the transducer surface (F_o) was sufficiently large to overcome the surface tension forces (F_s) in the larger pores of the fabric, resulting in rapid shedding of water from these pores. The shedding of a large fraction of water via ultrasonic excitation resulted in a non-linear decrease in the fabric water content. The fraction of water shedding in this region was dictated by the fraction of pores in the fabric with $F_o > F_s$, with the amount of water shedding increasing as the number of such pores increase. Based on the data presented in **Figure 9**, it can be deduced that fabric F-1 consist of a larger fraction of pores with $F_o > F_s$ than fabric F-2, resulting in a greater decrease in water content during the initial non-linear phase. This conclusion can also get the evidence from **Figure 4**, which fabric F-2 shows denser structure and smaller pores compared with fabric F-1. At the end of the non-linear phase, the only pores containing liquid were those with $F_s > F_o$. The continued excitation of the transducer surface caused the temperature of liquid trapped in these pores to rise via viscous dissipation without shedding water from the fabric. This response was similar to the thermal response of droplets observed when $F_s > F_o$. The increase in temperature of the liquid (and the fabric) induced thermal evaporation from the fabric, which caused a linear decrease in the fabric water content (similar to the trend presented in **Figure 8**).

Here, the kinematics of fabric drying on transducer B were similar to those of droplet atomization, where $F_s > F_o$ at $t^* = 0$. Therefore, the primary response of the liquid upon excitation was thermal, and the fabric temperature rapidly increased due to viscous dissipation. However, since the surface tension force (F_s) in the fabric was much greater than that of the 10 μ L droplet, the increase in temperature did not cause F_s to decrease below F_o . Therefore, ultrasonic drying was not induced on this transducer, resulting in the absence of a non-linear drying region. Compared with the thermal drying curves for different fabrics (**Figure 8**), it also indicates that the water shedding on transducer B was primarily driven by thermal evaporation. As in the case of thermal drying, the drying time of the F-1 fabric was shorter than that of the F-2 fabric.

In addition, the drying data suggest that a larger volume of water was shed from the fabric during the nonlinear regime on transducer C than on transducer A and, overall, fabrics dried more quickly on transducer C than on transducer A and B.

5. Ultrasonic drying behavior of fabric under burst-mode driving

A simple analysis of the dynamics of the contact between the fabric and ultrasonic transducer during the fabric drying process illustrates that the transducer does not need to be constantly on to obtain the same drying effect. As the transducer vibrates, it pushes the fabric upward. The fabric loses contact with the surface of the transducer. After some time, the fabric falls back onto the transducer due to the gravity. During the time when there is no contact between the fabric and the transducer, power is consumed with no contribution to the fabric drying [12]. Therefore, power can be supplied to the transducer in bursts rather than continuously without affecting the drying process, which can increase the energy efficiency.

The drying behavior of fabric F-1 at different duty cycles for a given modulating frequency on transducer C is presented in **Figure 10**. The fabric size was fixed at $4 \times 4 \text{ mm}^2$ and the initial water mass was 10 mg. The modulating frequency in **Figure 10a–b** is 100 and 1000 Hz, respectively. The drying behavior of the fabric with the modulating signal added keeps the same with the drying behavior of the fabric without modulating signal (represented by “No DC” in **Figure 10**), as illustrated in **Figure 10**. The total drying time increased from 20 to 30 s when the duty cycle was 20%. However, when the duty cycle was 40%, the drying time was 25 s and was 5 s less than the total drying time when the duty cycle was 20%, as

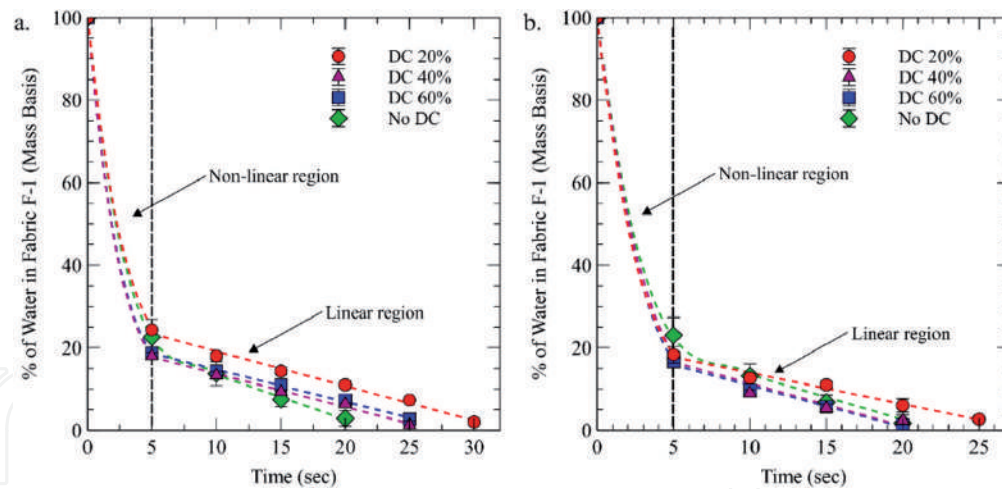


Figure 10.

Effect of duty cycle (DC) on the drying curves of fabric F-1 on transducer C. Modulating frequency: (a) 100 Hz and (b) 1000 Hz [12].

illustrated in **Figure 10(a)**. Increasing the duty cycle from 20 to 60% did not significantly affect the total drying time of the non-linear region of the drying curve. However, the slope of the linear region of the drying curve changed when the duty cycle was below 40%, resulting in an increase in the drying time.

When the transducer was turned on, because the ultrasonic excitation force of transducer C was much larger than the surface tension force of water in the large pores (i.e., $R > 1$), regardless of the duty cycle, the water accumulated in the large pores could be ejected quickly. However, water accumulated in the small pores experienced a larger surface tension force than the ultrasonic excitation force ($R < 1$). Therefore, the non-linear region of the drying behavior corresponded to water removal from the large pores while the linear region corresponded to drying in the small pores. In addition, in **Figure 10(a)**, it illustrates that adding the duty cycle did not change the nonlinear region of the drying process, but it changed the linear region of the drying process. This is also because the water embedded in the larger pores was easier to be atomized immediately after the transducer was actuated. As illustrated in **Figure 10(a)**, compared with the drying time in the nonlinear region, the drying time of the linear region was 3 times of that in the nonlinear region which there was no duty cycle added although the water percentage in the linear region was just 25% of the nonlinear region. For the duty cycle added, the linear region took even longer time compared with no duty cycle added. This is because the power in this situation was not continuously turned on and was determined by the duty cycle. The water in the fibers was even harder to be taken out by the atomization effect than the situation when there was no duty cycle. From the above analysis, it can be concluded that the duty cycle did not affect the water accumulated in the larger pores, but it affected the water accumulated in the small pores. These conclusions can also be arrived from **Figure 10(b)**.

As can be seen from **Figure 10**, it illustrates that when the duty cycle increased from 20 to 40%, the drying time decreased. The drying time also changed when the duty cycle kept the same but the modulation frequency changed. Such as, when the duty cycle was 20%, the drying time was 30 s at 100 Hz modulation frequency, but at 1000 Hz modulation frequency the drying time was 25 s. Therefore, both the duty cycle and modulation frequency of the modulating signal affected the drying time of the fabric.

The effects of different duty cycles and modulating frequencies on the drying time of a $4 \times 4 \text{ mm}^2$ swatch of fabric F-1 on transducer C is presented in **Figure 11a**. The initial water mass was fixed at 10 mg. At a 100% duty cycle, the drying time was 20 s, irrespective of modulating frequency (**Figure 11a**). This value is identical to the drying time obtained when the transducer was continuously driven. The results here

demonstrate that the drying time cannot be decreased by changing the duty cycle; however, the power consumed by the transducer can be lowered by doing so [12].

To understand the effects of duty cycle and modulating frequency on fabric drying times, the drying time of a $5 \times 5 \text{ mm}^2$ swatch of fabric F-1 was also studied on transducer C. The initial water mass was fixed at 15 mg. The results of these experiments are presented in **Figure 11b**. The results demonstrate that reducing the modulating frequency increased the drying time of fabric [12]. Furthermore, at a given modulating frequency, the drying time decreased as the duty cycle was increased up to a duty cycle D_0 . Increasing the duty cycle beyond this value of D_0 did not change the drying time. The results also indicate that the value of D_0 is dependent on the modulating frequency, such that D_0 increased as the modulating frequency decreased. As shown in **Figure 11b**, $D_0 = 60\%$ for a modulating frequency of 1000 Hz, and $D_0 = 80\%$ for a modulating frequency of 700 Hz. This implies that at a given modulating frequency, the energy consumption can be reduced without affecting the drying time by operating the transducer at a duty cycle D_0 .

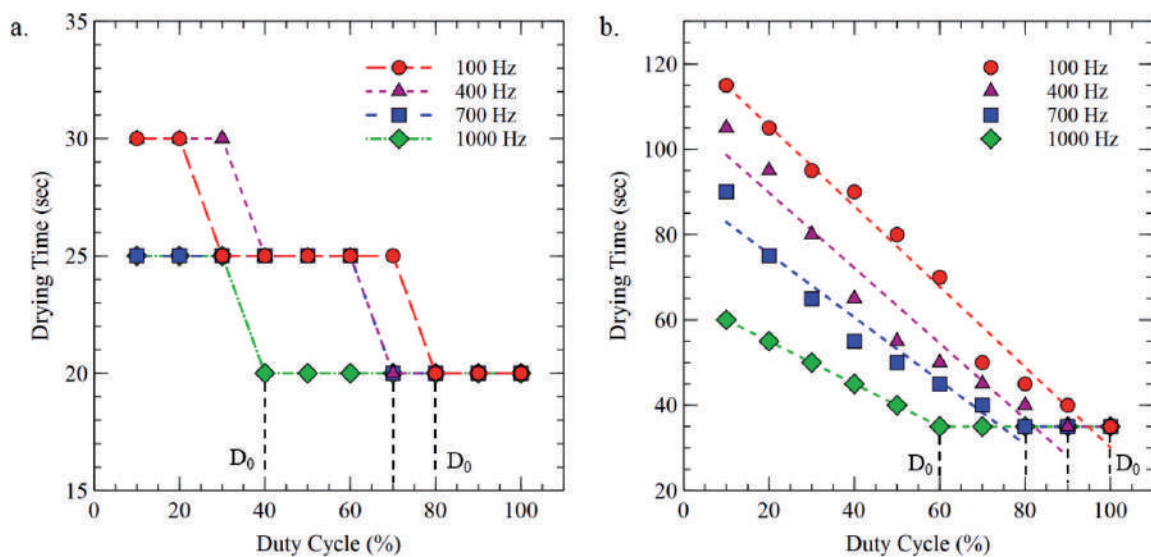


Figure 11. Effects of duty cycle on the drying time of fabric F-1 on transducer C. Fabric size: (a) $4 \times 4 \text{ mm}^2$ and (b) $5 \times 5 \text{ mm}^2$ [12].

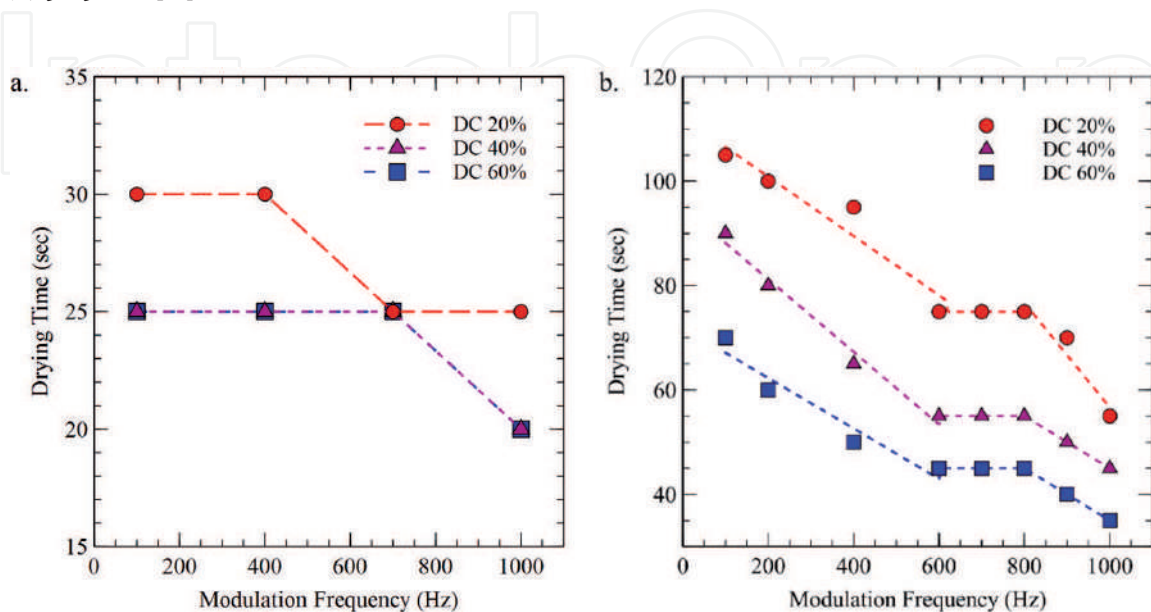


Figure 12. Effects of modulating frequency on the drying time for fabric F-1 on transducer C. Fabric size: (a) $4 \times 4 \text{ mm}^2$ and (b) $5 \times 5 \text{ mm}^2$ [12].

The effects of modulating frequency on the drying time of a 4×4 and a 5×5 mm² swatch of fabric F-1 on transducer C are presented in **Figure 12a–b**. The initial water mass for the 4×4 and 5×5 mm² pieces of fabric were 10 and 15 mg, respectively.

As seen in **Figure 12a**, since the difference of drying times at different modulation frequencies were relatively small, such as for the duty cycle 40%, the drying time at 100 Hz modulating frequency was 25 s and at 1000 Hz modulating frequency the drying time was 20 s, the drying time kept the same at certain modulating frequency. But following that modulating frequency, the drying time decreased linearly with the increase of the modulating frequency. Also, **Figure 12b** illustrates that the drying time reduced with the increase of modulating frequency. These conclusions can also be derived from the data in **Figure 11**.

6. Energy efficiency analysis

The EF ($EF_{100-20\%}$) values for the drying of fabric F-1 at different drying conditions were compared (**Table 5**). The duty cycle and modulating frequency corresponding to each drying condition are shown in **Table 5**. Drying type A refers to fabric F-1 drying on transducer A; drying types C1–C5 refer to fabric F-1 drying

Drying types	Duty cycle (%)	Modulating frequency (Hz)	$EF_{100-20\%}$ (lb/kWh)
A	Continuous driving mode		0.27
C1	Continuous driving mode		2.79
C2	10	100	19.01
C3	10	400	19.01
C4	10	700	26.61
C5	10	1000	44.35

Table 5. Comparison of energy factors (EF) for drying fabric F-1 at different drying conditions [12].

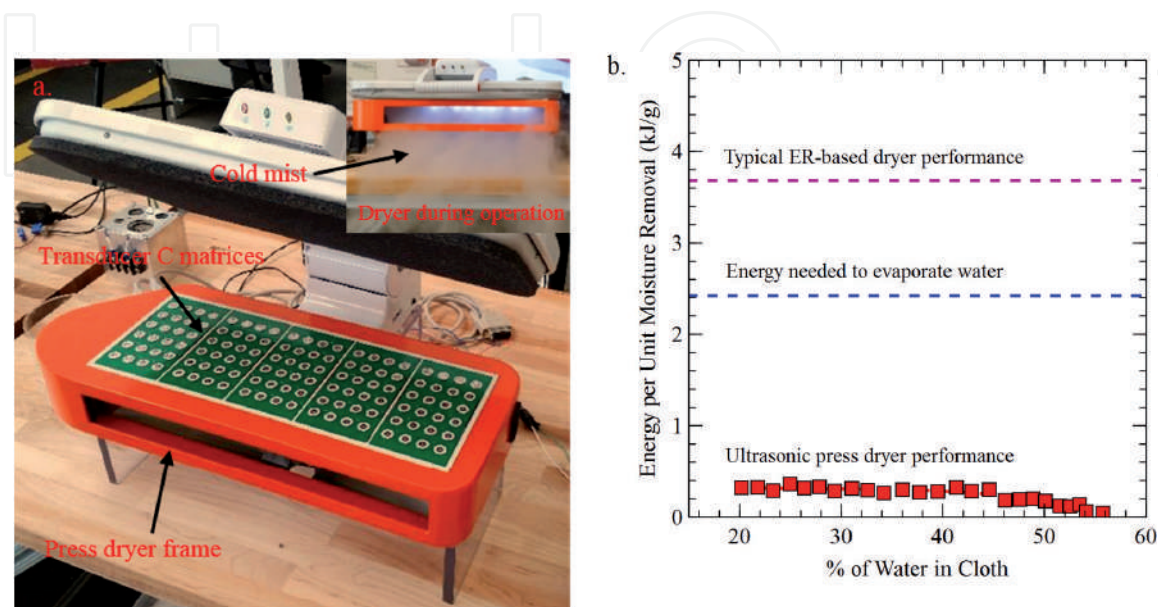


Figure 13. (a) A mid-scale press type ultrasonic clothes dryer, and (b) its energy consumption data at different initial water content [11].

on transducer C. As illustrated in **Figures 11** and **12**, the drying time for fabric F-1 dropped with an increase in the modulating frequency and duty cycle up to D_0 . The $EF_{100-20\%}$ values at different modulating frequencies with the duty cycle fixed at 10% (shortest duty cycle in the tests) were calculated and compared with continuous transducer driving (**Table 5**). The values in **Table 5** show that $EF_{100-20\%}$ values for the new drying method with modulating signals are about 7–16 times greater than those for continuous transducer driving.

A mid-scale press type ultrasonic cloth dryer was designed and fabricated, for which the ultrasonic transducer C was utilized due to its best drying performance among all the three transducers. **Figure 13a** shows the demonstration unit of this ultrasonic press dryer, which a shirt size cloth can be dried by this unit. The energy consumption per unit mass of water content (kJ/g) removed from the fabric by this ultrasonic press dryer was tested. The energy efficiency of it was compared with the latent heat of evaporation for water (at ambient temperature and pressure) and the typical electric resistance (ER)-based dryer (**Figure 13b**). The results show that the energy efficiency of the ultrasonic drying process is much higher than the thermal evaporation and ER-based drying method. Compared with the typical ER-based dryer, the energy efficiency of this ultrasonic press dryer is more than 10 times higher.

7. Conclusion

In this chapter, high-frequency, direct-contact vibrational drying of fabrics using ultrasonic transducers have been introduced as a promising technology to reduce both the drying time and energy consumption of the drying process. The physical mechanism of fabric drying was comprehensively analyzed. The results showed that the fabric drying processes consist of nonlinear and linear regimes, which were dominated by ultrasonic vibration and thermal evaporation, respectively. The electric power could be supplied to ultrasonic transducer in burst mode rather than continuously, saving energy but not affecting the drying processes. Operating the transducer on a shorter duty cycle and at a higher modulating frequency was more energy-efficient for fabric drying. Based on the initial tests on a press type ultrasonic clothes dryer, this direct-contact ultrasonic drying technique showed energy efficiency more than 10 times higher than a typical electrical resistance dryer, and 5 times higher than the latent heat of evaporation at water content greater than 20%.

Acknowledgements

The author would like to express sincere gratitude to Prof. Saeed Moghaddam in Department of Mechanical and Aerospace Engineering, University of Florida, for his support during the research work in University of Florida.

The author also would like to acknowledge support from Oak Ridge National Laboratory for its assistance.

Conflict of interest

The author declares that there are no affiliations with or involvement in any organization or entity with any financial interest or non-financial interest in the subject matter or material discussed in this manuscript.

IntechOpen

IntechOpen

Author details

Chang Peng* and Saeed Moghaddam
Department of Mechanical and Aerospace Engineering, University of Florida,
Gainesville, FL, USA

*Address all correspondence to: chang.peng@ufl.edu

IntechOpen

© 2019 The Author(s). Licensee IntechOpen. This chapter is distributed under the terms of the Creative Commons Attribution License (<http://creativecommons.org/licenses/by/3.0>), which permits unrestricted use, distribution, and reproduction in any medium, provided the original work is properly cited. 

References

- [1] How Much Electricity Do Appliances Use? Off Energy Effic Renew Energy. 2015. Available at: <https://energy.gov/energysaver/appliances-and-electronics>
- [2] Denkenberger D, Calwell C, Beck N, Trimboli B. Analysis of potential energy savings from heat pump clothes dryers in North America. CLASP. 2013;1-42. Available at: <http://clasp.ngo/Resources/Resources/PublicationLibrary/2013/Clothes-Dryer-Heat-Pump-Technology-Offers-Substantial-Cost-and-Energy-Savings-for-North-America>
- [3] U.S. Environmental Protection Agency. Market & industry scoping report: Residential clothes dryers. Energy Star. 2011;1-18. Available at: https://www.energystar.gov/sites/default/files/asset/document/ENERGY_STAR_Scoping_Report_Residential_Clothes_Dryers.pdf
- [4] Zegers FTS, Molenbroek EC. Field Test of Heat-Fed Washing Machines and Tumble Dryers. Utrecht: ECOFYS; 2000
- [5] Lekov A, Franco V, Meyers S. Evaluation of energy efficiency standards for residential clothes dryers in the USA. Energy Efficiency. 2014;7:133-149
- [6] Caldeira KG, Chan AK, Hyde RA, Kare JT, Myhrvold NP, Whitmer C, et al. Energy efficient dryer systems. US 9091015 B2; 2015
- [7] Lakkineni VR, Zentner MM, Anikhindi SM, Froelicher SB, Jr ON, MTB, et al. Energy efficient cycle for clothes dryer. US 8991068 B2; 2015
- [8] Martin E, Sutherland K, Parker D. Measured performance of heat pump clothes dryers. ACEEE Summer Study Energy Efficiency in Buildings. 2016;2016:1-13
- [9] Yoon C-H. Microwave clothes dryer. U.S. Patent No. 1988;4:765,066
- [10] McCarthy DE. Apparatus for drying clothes or other solids using microwave energy under reduced pressure with energy recovery while avoiding arcing. U.S. Patent Application No. 2013;13(/783):198
- [11] Peng C, Ravi S, Patel VK, Momen AM, Moghaddam S. Physics of direct-contact ultrasonic cloth drying process. Energy. 2017;125:498-508
- [12] Peng C, Momen AM, Moghaddam S. An energy-efficient method for direct-contact ultrasonic cloth drying. Energy. 2017;138:133-138
- [13] Deepu P, Peng C, Moghaddam S. Dynamics of ultrasonic atomization of droplets. Experimental Thermal and Fluid Science. 2018;92:243-247
- [14] Peng C, Moghaddam S. Energy efficient piezoelectrically actuated transducer for direct-contact ultrasonic drying of fabrics. Drying Technology. 2019;1-10
- [15] Patel VK, Reed FK, Kisner R, Peng C, Moghaddam S, Momen AM. Novel experimental study of fabric drying using direct-contact ultrasonic vibration. Journal of Thermal Science and Engineering Applications. 2019;11:021008
- [16] Jaffe B, Cook WR, Jaffe H. Piezoelectric Ceramics. New York: Academic Press; 1971
- [17] Khmelev VN, Savin II, Abramenko DS, Tsyganok SN, Barsukov RV, Lebedev AN. Research the acoustic cloth drying process in mock-up of drum-type washing machine. International Workshops and Tutorials on Electron Devices and Materials EDM—Proceedings. 2006:223-228

[18] Khmelev VN, Barsukov RV, Abramenko DS, Genne DV. Research and development of ultrasonic device prototype for intensification of drying process. International Workshops and Tutorials on Electron Devices and Materials EDM—Proceedings. 2008;235-240

[19] Patnaik A, Rengasamy RS, Kothari VK, Ghosh A. Wetting and wicking in fibrous materials. Textile Progress. 2006;38:1-105

IntechOpen